ELASTIC SCATTERER RECONSTRUCTION VIA THE REGULARIZED SAMPLING METHOD

S. NINTCHEU FATA * AND B. B. GUZINA†

Abstract. A three-dimensional inverse problem dealing with the reconstruction of cavities in a uniform semi-infinite solid from surface elastodynamic waveforms is investigated via the linear sampling method. To cater for active imaging applications that are often characterized by a limited density of illuminating sources, the existing near-field formulation of the linear sampling method is advanced in terms of its adjoint statement that features integration over the receiver surface rather than its source counterpart. To deal with an ill-posedness of the integral equation that is used to reconstruct the obstacle, the problem is solved by alternative means of Tikhonov regularization and a preconditioned conjugate gradient method. Computational details of the imaging procedure, including evaluation of the featured integrals as well as the implementation of the regularization approach, are highlighted. An example dealing with the reconstruction of an ellipsoidal void from noise-polluted synthetic measurements is included to illustrate the effectiveness of the proposed methodology.

Key words. Inverse scattering, elastic waves, ill-posed problems, conjugate gradient, half-space

AMS subject classifications. 35R30, 65R30, 74J05, 74J20

1. Introduction. Remote sensing of subsurface obstacles using elastic waves with "long" wavelengths (i.e. those inside the so-called resonance region [9]) is an inverse scattering problem relevant to a variety of applications such as non-destructive material testing, hydrocarbon prospecting, and medical diagnosis. In the context of seismic inversion, such low-frequency waveforms are often interpreted by means of the full waveform tomography [33] which typically couples gradient-based, nonlinear minimization with finite-difference (forward) simulation of elastic wave propagation [5, 32]. For simple (e.g. homogeneous) background media, the waveform tomography approach to seismic imaging can be alternatively established within the framework of elastodynamic boundary integral equation (BIE) methods, especially when aided by the analytical sensitivity estimates [3, 16]. Irrespective of the type of forward model, however, the high resolution of full waveform inversion is commonly balanced by its lack of robustness, manifest in the convergence of underlying minimization to local minima [28, 33].

Over the past decade, Colton et al. [8, 10, 12] introduced an alternative, point-probing technique for solving inverse scattering problems in acoustics and electromagnetics, the so-called linear sampling method (LSM) that circumvents many of the foregoing impediments. This minimization-free approach to waveform tomography makes use of an ill-posed integral equation, written with reference to the obstacle-free domain, whose kernel is constructed from the observed waveforms and whose solution norm (used as an obstacle indicator) remains bounded *only* for sampling points striking the support of the scatterer. Owing to its computational efficiency and relative robustness (stemming from the absence of nonlinear optimization), the LSM has since been adapted to both far-field [1, 6, 31] and near-field [29] elastic scattering problems. Despite its inherent appeal however, the existing formulation of the LSM for near-field elastodynamics [29] which postulates integration over the source region, may not be

*Computer Science and Mathematics Division, Oak Ridge National Laboratory, Oak Ridge, TN 37831, USA (nintcheufats@ornl.gov).

†Department of Civil Engineering, University of Minnesota, Minneapolis, Minnesota 55455, USA (guzina@wave.ce.umn.edu). Corresponding author.

applicable to testing configurations that are characterized by a limited density of "illuminating" sources (e.g. magnetic resonance elastography [20, 13]). Due to the fact that the featured (ill-posed) integral equation is usually solved in terms of singular value decomposition, application of the available sampling algorithm to imaging situations involving a large number of observations (i.e. waveform measurements) may further lead to substantial computational cost and inaccurate singular values.

To transcend the foregoing impediments, the focus of this study is two-fold and includes: (i) a reformulation of the LSM for near-field elastodynamics that caters to active imaging configurations with only a limited density of excitation sources, and (ii) employment of a numerical algorithm for solving ill-conditioned linear systems that establishes an alternative to singular value decomposition. To this end, an *adjoint statement* of the sampling method in [29] is proposed wherein the inverse problem is formulated as a linear integral equation of the first kind, involving integration over the *measurement* (as opposed to the source) surface, whose solution becomes unbounded in the exterior of a hidden scatterer. A preconditioned conjugate-gradient algorithm for solving ill-posed linear systems, established earlier for X-ray computed tomography [34], is further employed to elevate the performance of the linear sampling method. A set of examples with noise-polluted synthetic measurements is included to illustrate the performance of the method.

2. Problem formulation. This investigation deals with time-harmonic, elastic wave imaging of a bounded obstacle $\Omega_{\rm C}$ that is strictly embedded in a uniform, isotropic semi-infinite solid (see Fig. 2.1). In the sequel, the obstacle is assumed to have a smooth boundary Γ of class $C^{1,\alpha}$, $\alpha\in(0,1]$. Adopting the hypothesis of an "impenetrable" scatterer, $\Omega_{\rm C}$ is further assumed to be in the form of a *cavity*. With reference to the Cartesian frame $\{O;\xi_1,\xi_2,\xi_3\}$ set at the top of the half-space, the semi-infinite background domain $\Omega=\{(\xi_1,\xi_2,\xi_3)|\,\xi_3>0\}$ is characterized by the Lamé constants λ and μ, and mass density ρ; its free surface $\{(\xi_1,\xi_2,\xi_3)|\,\xi_3=0\}$ is denoted by Σ. For further reference, let $\Omega^-=\Omega\setminus(\Omega_{\rm C}\cup\Gamma)$ denote the unbounded region surrounding the obstacle, and let Γ_R be a hemisphere centered at the origin O. The respective subset of Ω and Ω^- that are bounded by Γ_R are denoted by Ω_R and Ω_R^-, with an implicit assumption that R is sufficiently large such that $\Omega_{\rm C}\subset\Omega_R$. As implied by the Figure, the scatterer $\Omega_{\rm C}$ is exposed by time-harmonic sources acting on the "source" surface $\Gamma_1\subset\Sigma$, with the induced half-space motion monitored over the "measurement" area $\Gamma_2\subset\Sigma$. In what follows the frequency of excitation is denoted by ω, with the implicit time-harmonic factor $\mathrm{e}^{\mathrm{i}\omega t}$ omitted for brevity.

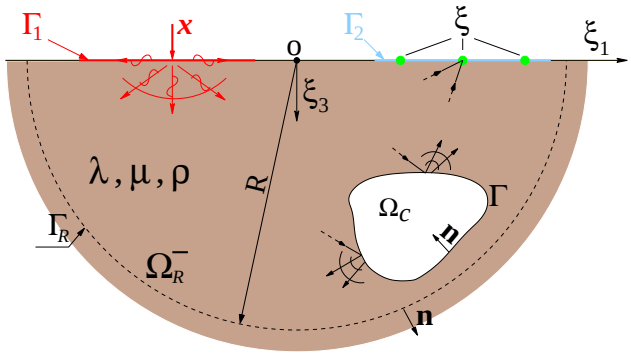

FIG. 2.1. *Illumination of a hidden obstacle by elastic waves.*

2.1. Direct scattering problem. In situations where the excitation source used to illuminate the obstacle is a *point force* of unit magnitude acting at $\boldsymbol{x}\in\Gamma_1$ in the kth coordinate direction, the elastodynamic displacement response of the semi-infinite solid Ω^- can be conveniently decomposed as

$$\boldsymbol{u}^k(\boldsymbol{\xi},\boldsymbol{x}) \,=\, \mathring{\boldsymbol{u}}^k(\boldsymbol{\xi},\boldsymbol{x}) + \tilde{\boldsymbol{u}}^k(\boldsymbol{\xi},\boldsymbol{x}), \qquad \boldsymbol{\xi}\in\Omega^-, \quad \boldsymbol{x}\in\Gamma_1, \tag{2.1}$$

where $\tilde{\boldsymbol{u}}^k$ represents the scattered field ($\tilde{\boldsymbol{u}}^k=\boldsymbol{0}$ in the absence of a scatterer) and $\mathring{\boldsymbol{u}}^k$ denotes the free field, i.e. the response of the obstacle-free solid Ω to prescribed excitation. With such definitions, one has

$$\mathring{\boldsymbol{u}}^k(\boldsymbol{\xi},\boldsymbol{x}) = \hat{\boldsymbol{u}}^k(\boldsymbol{\xi},\boldsymbol{x}), \quad \boldsymbol{\xi}\neq\boldsymbol{x}, \quad \boldsymbol{\xi}\in\Omega, \quad \boldsymbol{x}\in\Gamma_1, \tag{2.2}$$

where $\hat{\boldsymbol{u}}^k(\boldsymbol{\xi},\boldsymbol{x})$ is the elastodynamic displacement Green's function for a homogeneous isotropic half-space at $\boldsymbol{\xi}\in\Omega$ due to a unit time-harmonic point force acting at $\boldsymbol{x}\in\Gamma_1$ in the kth direction (e.g. [15]).

With reference to any smooth surface $S\subset\Omega$ with unit normal $\boldsymbol{n}$, it is further useful to introduce the traction vector

$$\boldsymbol{t}(\boldsymbol{\xi};\boldsymbol{u}) = \boldsymbol{n}(\boldsymbol{\xi})\cdot\mathbf{C}\colon\boldsymbol{\nabla}\boldsymbol{u}(\boldsymbol{\xi}), \quad \boldsymbol{\xi}\in S, \tag{2.3}$$

associated with displacement field $\boldsymbol{u}$, where $\mathbf{C} = \lambda\,\mathbf{I}_2\otimes\mathbf{I}_2 + 2\,\mu\,\mathbf{I}_4$, denotes the isotropic elasticity tensor and $\mathbf{I}_k$ ($k=2,4$) is the symmetric kth order identity tensor.

On the basis of (2.1)–(2.3), the forward problem associated with Fig. 2.1 can be specified as a task of resolving the scattered field, $\tilde{\boldsymbol{u}}^k$, from the knowledge of the free field $\mathring{\boldsymbol{u}}^k$ and the exact geometry of the (prescribed impenetrable) scatterer Ω_{c}. More precisely, one is to find $\tilde{\boldsymbol{u}}^k\in C^2(\Omega^-)\cap C^1(\Omega^-\cup\Gamma\cup\Sigma)$ that satisfies the homogeneous Navier equation

$$\boldsymbol{L}\tilde{\boldsymbol{u}}^k(\boldsymbol{\xi},\boldsymbol{x}) + \rho\omega^2\tilde{\boldsymbol{u}}^k(\boldsymbol{\xi},\boldsymbol{x}) = \boldsymbol{0}, \quad \boldsymbol{\xi}\in\Omega^-, \quad \boldsymbol{x}\in\Gamma_1, \tag{2.4}$$

and Neumann boundary conditions

$$\tilde{\boldsymbol{t}}^k(\boldsymbol{\xi},\boldsymbol{x}) = \begin{cases} \boldsymbol{0}, & \boldsymbol{\xi}\in\Sigma, \\ -\mathring{\boldsymbol{t}}^k(\boldsymbol{\xi},\boldsymbol{x}), & \boldsymbol{\xi}\in\Gamma, \end{cases} \qquad \boldsymbol{x}\in\Gamma_1, \tag{2.5}$$

where $\mathring{\boldsymbol{t}}^k = \boldsymbol{t}(\boldsymbol{\xi};\mathring{\boldsymbol{u}}^k)$; $\tilde{\boldsymbol{t}}^k = \boldsymbol{t}(\boldsymbol{\xi};\tilde{\boldsymbol{u}}^k)$ is understood in the sense of the trace [26], and $\boldsymbol{L} = \mu\boldsymbol{\nabla}^2 + (\lambda+\mu)\boldsymbol{\nabla}\boldsymbol{\nabla}\cdot$ is the Lamé operator. For the well-posedness of the forward scattering problem, the scattered field $\tilde{\boldsymbol{u}}^k$ must also satisfy with the generalized radiation condition

$$\lim_{R\to\infty}\int_{\Gamma_R}\left\{\hat{\boldsymbol{u}}^j(\boldsymbol{\xi},\boldsymbol{x})\cdot\tilde{\boldsymbol{t}}^k(\boldsymbol{\xi},\boldsymbol{x}) - \hat{\boldsymbol{t}}^j(\boldsymbol{\xi},\boldsymbol{x})\cdot\tilde{\boldsymbol{u}}^k(\boldsymbol{\xi},\boldsymbol{x})\right\}dS_{\boldsymbol{\xi}} = 0, \quad \boldsymbol{x}\in\Omega_R^-, \tag{2.6}$$

common to all radiating solutions in Ω^- [16]. In (2.6), $\hat{\boldsymbol{t}}^j(\boldsymbol{\xi},\boldsymbol{x}) = \boldsymbol{t}(\boldsymbol{\xi};\hat{\boldsymbol{u}}^j)$ is the traction vector at $\boldsymbol{\xi}\in\Gamma_R$ associated with $\hat{\boldsymbol{u}}^j(\boldsymbol{\xi},\boldsymbol{x})$, i.e., the elastodynamic traction Green's function for a uniform isotropic half-space. Throughout this investigation, it is assumed that the forward scattering problem for the semi-infinite solid Ω^- given by (2.4), (2.5) and (2.6) admits a unique solution $\tilde{\boldsymbol{u}}^k\in H^1_{loc}(\Omega^-)$.

2.2. Inverse scattering problem. To formulate the reconstruction method, it is instructive to introduce the *Green's tensor* $\widehat{\boldsymbol{U}}(\boldsymbol{\xi},\boldsymbol{x})$ and the *scattered tensor* $\widetilde{\boldsymbol{U}}(\boldsymbol{\xi},\boldsymbol{x})$, both associated with a unit point source acting at $\boldsymbol{x}\in\Gamma_1$. In the reference Cartesian frame, components of $\widehat{\boldsymbol{U}}(\boldsymbol{\xi},\boldsymbol{x})$ can be arranged in a 3×3 matrix

$$\widehat{\boldsymbol{U}}(\boldsymbol{\xi},\boldsymbol{x})=\begin{pmatrix}\hat{u}_1^1(\boldsymbol{\xi},\boldsymbol{x}) & \hat{u}_1^2(\boldsymbol{\xi},\boldsymbol{x}) & \hat{u}_1^3(\boldsymbol{\xi},\boldsymbol{x})\\ \hat{u}_2^1(\boldsymbol{\xi},\boldsymbol{x}) & \hat{u}_2^2(\boldsymbol{\xi},\boldsymbol{x}) & \hat{u}_2^3(\boldsymbol{\xi},\boldsymbol{x})\\ \hat{u}_3^1(\boldsymbol{\xi},\boldsymbol{x}) & \hat{u}_3^2(\boldsymbol{\xi},\boldsymbol{x}) & \hat{u}_3^3(\boldsymbol{\xi},\boldsymbol{x})\end{pmatrix},\quad \boldsymbol{\xi}\in\Omega\backslash\{\boldsymbol{x}\},\quad \boldsymbol{x}\in\Gamma_1, \tag{2.7}$$

where $\hat{\boldsymbol{u}}^k=(\hat{u}_1^k,\hat{u}_2^k,\hat{u}_3^k)$ is the elastodynamic displacement Green's function for the semi-infinite solid Ω as examined before. Here it is useful to note that $\widehat{\boldsymbol{U}}$ is characterized by the reciprocity property [16], i.e. that $\widehat{\boldsymbol{U}}(\boldsymbol{\xi},\boldsymbol{x})=\left[\widehat{\boldsymbol{U}}(\boldsymbol{x},\boldsymbol{\xi})\right]^{\mathrm{T}}$ $(\boldsymbol{x}\neq\boldsymbol{\xi},\quad \boldsymbol{x},\boldsymbol{\xi}\in\Omega)$ where superscript "$^{\mathrm{T}}$" denotes the matrix transpose.

By analogy to (2.7), the perturbation of $\widehat{\boldsymbol{U}}$ due to presence of the scatterer can be written in the form of the scattered tensor

$$\widetilde{\boldsymbol{U}}(\boldsymbol{\xi},\boldsymbol{x})=\begin{pmatrix}\tilde{u}_1^1(\boldsymbol{\xi},\boldsymbol{x}) & \tilde{u}_1^2(\boldsymbol{\xi},\boldsymbol{x}) & \tilde{u}_1^3(\boldsymbol{\xi},\boldsymbol{x})\\ \tilde{u}_2^1(\boldsymbol{\xi},\boldsymbol{x}) & \tilde{u}_2^2(\boldsymbol{\xi},\boldsymbol{x}) & \tilde{u}_2^3(\boldsymbol{\xi},\boldsymbol{x})\\ \tilde{u}_3^1(\boldsymbol{\xi},\boldsymbol{x}) & \tilde{u}_3^2(\boldsymbol{\xi},\boldsymbol{x}) & \tilde{u}_3^3(\boldsymbol{\xi},\boldsymbol{x})\end{pmatrix},\quad \boldsymbol{\xi}\in\Omega^-,\quad \boldsymbol{x}\in\Gamma_1, \tag{2.8}$$

where and $\tilde{u}_j^k$ is the j-th Cartesian components of the scattered field at $\boldsymbol{\xi}\in\Omega^-$ due to a unit point source acting at $\boldsymbol{x}\in\Gamma_1$ in the k-th coordinate direction so that $\tilde{\boldsymbol{u}}^k=(\tilde{u}_1^k,\tilde{u}_2^k,\tilde{u}_3^k)$.

With reference to (2.3) and (2.7), it is also useful to introduce the *traction Green's tensor*

$$\widehat{\boldsymbol{T}}(\boldsymbol{\xi},\boldsymbol{x})=\boldsymbol{n}(\boldsymbol{\xi})\cdot\mathbf{C}:\boldsymbol{\nabla}_{\boldsymbol{\xi}}\widehat{\boldsymbol{U}}(\boldsymbol{\xi},\boldsymbol{x}),\quad \boldsymbol{\xi}\in S\backslash\{\boldsymbol{x}\},\quad \boldsymbol{x}\in\Gamma_1, \tag{2.9}$$

for any smooth surface $S\subset\Omega$ with unit normal $\boldsymbol{n}$.

With the above definitions, the inverse problem of interest can be specified as a task of reconstructing an impenetrable obstacle Ω_{C} from the knowledge of the scattered tensor $\widetilde{\boldsymbol{U}}(\boldsymbol{\xi},\boldsymbol{x})$ for *all* observation points $\boldsymbol{\xi}\in\Gamma_2\subset\Sigma$ and *all* source points $\boldsymbol{x}\in\Gamma_1\subset\Sigma$. In what follows, this problem will be solved by generalizing upon the linear sampling method for near-field elastodynamics proposed in [29] that assumes continuous representation of $\widetilde{\boldsymbol{U}}(\boldsymbol{\xi},\boldsymbol{x})$ as an experimental input. In practice, however, $\widetilde{\boldsymbol{U}}$ is constructed using spatially discrete measurements which necessitates a sufficient density of source and observation points. One of the key objectives in this study is to relax the former requirement in terms of the density of excitation sources through a rigorous mathematical reformulation of the existing technique.

3. Preliminaries. Initially developed by Colton and Kirsch [8] in the context of far-field acoustics, the linear sampling method for the *full waveform* (i.e. near-field) obstacle identification in elastodynamics was shown in [29] to revolve around the linear integral equation of the first kind

$$(\boldsymbol{F}\boldsymbol{g}_{\boldsymbol{z},\boldsymbol{d}})(\boldsymbol{\xi})=\widehat{\boldsymbol{U}}(\boldsymbol{\xi},\boldsymbol{z})\cdot\boldsymbol{d},\quad \boldsymbol{\xi}\in\Gamma_2,\quad \boldsymbol{z}\in\Omega,\quad \boldsymbol{d}\in\mathbb{R}^3,\quad \|\boldsymbol{d}\|=1, \tag{3.1}$$

where the near-field operator $\boldsymbol{F}\colon L_2(\Gamma_1)\to L_2(\Gamma_2)$ is defined as

$$(\boldsymbol{F}\boldsymbol{g}_{\boldsymbol{z},\boldsymbol{d}})(\boldsymbol{\xi}):=\int_{\Gamma_1}\widetilde{\boldsymbol{U}}(\boldsymbol{\xi},\boldsymbol{x})\cdot\boldsymbol{g}_{\boldsymbol{z},\boldsymbol{d}}(\boldsymbol{x})\,dS_{\boldsymbol{x}},\quad \boldsymbol{\xi}\in\Gamma_2; \tag{3.2}$$

$\widetilde{\boldsymbol{U}}$ synthesizes the experimental observations; $\boldsymbol{g}_{\boldsymbol{z},\boldsymbol{d}}(\cdot) \equiv \boldsymbol{g}(\cdot;\boldsymbol{z},\boldsymbol{d}) \in L_2(\Gamma_1)$ is the unknown vector density, and $\boldsymbol{d}$ is a unit vector signifying polarization of the "fictitious" point source (the right-hand side of (3.1)) acting at the *sampling point* $\boldsymbol{z}$. Here $L_2(S)$ denotes the Hilbert space of square-integrable vector fields equipped with the inner product

$$(\boldsymbol{g},\boldsymbol{h})_{L_2(S)} = \int_S \overline{\boldsymbol{g}}(\boldsymbol{x}) \cdot \boldsymbol{h}(\boldsymbol{x})\, dS_{\boldsymbol{x}}, \tag{3.3}$$

overbar implies complex conjugation, and $S \subset \Sigma$ is a generic planar surface of finite extent. In the sequel, it is assumed that $\boldsymbol{d} \in \mathbb{R}^3$ and $\|\boldsymbol{d}\| = 1$.

For sampling points inside the support of the obstacle, i.e. $\boldsymbol{z} \in \Omega_{\mathrm{C}}$, it can be demonstrated that the ill-posed, full-waveform equation (3.1) possesses a unique solution $\boldsymbol{g}_{\boldsymbol{z},\boldsymbol{d}}$, and that $\|\boldsymbol{g}_{\boldsymbol{z},\boldsymbol{d}}\|_{L_2(\Gamma_1)}$ becomes unbounded as the sampling point $\boldsymbol{z} \in \Omega_{\mathrm{C}}$ approaches the boundary Γ of the scatterer Ω_{C} from its interior [29]. Using the concept of topological derivative [17], it is also shown that $\|\boldsymbol{g}_{\boldsymbol{z},\boldsymbol{d}}\|_{L_2(\Gamma_1)}$ can be made arbitrarily large when $\boldsymbol{z}$ lies outside of the support of the scatterer, i.e. $\boldsymbol{z} \in \Omega^-$. This unboundedness behavior of $\boldsymbol{g}_{\boldsymbol{z},\boldsymbol{d}}$ has prompted the use of $1/\|\boldsymbol{g}_{\boldsymbol{z},\boldsymbol{d}}\|_{L_2(\Gamma_1)}$, $\boldsymbol{z} \in \Omega$ as a characteristic function of the hidden obstacle Ω_{C}.

Unfortunately, single-layer representation (3.2) and thus integral equation (3.1) do not make much sense if the density of source points on the source surface Γ_1 is insufficient, a situation that is common to many physical testing configurations. To mitigate the problem, it is useful to consider an alternative statement of the linear sampling method wherein the integrals involved are taken over the observation surface Γ_2 rather than the source surface Γ_1.

For the ensuing developments, it is useful to recall Betti's integral identities of linear elasticity [23]. To this end, let D be a homogeneous, isotropic elastic body with boundary ∂D of class $C^{1,\alpha}$, and let $\boldsymbol{n}$ denote the unit outward normal to ∂D. With such premise Betti's first, second, and third formula for vector fields $\boldsymbol{u}, \boldsymbol{v} \in C^2(D) \cap C^1(\overline{D})$ can be written respectively as

$$\begin{aligned}
\int_D \boldsymbol{v}(\boldsymbol{\xi}) \cdot \boldsymbol{L}\boldsymbol{u}(\boldsymbol{\xi})\, dV_{\boldsymbol{\xi}} &= \int_{\partial D} \boldsymbol{v}(\boldsymbol{\xi}) \cdot \boldsymbol{t}(\boldsymbol{\xi};\boldsymbol{u})\, dS_{\boldsymbol{\xi}} - \int_D \boldsymbol{\nabla}\boldsymbol{v}(\boldsymbol{\xi}) : \mathbf{C} : \boldsymbol{\nabla}\boldsymbol{u}(\boldsymbol{\xi})\, dV_{\boldsymbol{\xi}}, \\
\int_D \boldsymbol{u}(\boldsymbol{\xi}) \cdot \boldsymbol{L}\boldsymbol{u}(\boldsymbol{\xi})\, dV_{\boldsymbol{\xi}} &= \int_{\partial D} \boldsymbol{u}(\boldsymbol{\xi}) \cdot \boldsymbol{t}(\boldsymbol{\xi};\boldsymbol{u})\, dS_{\boldsymbol{\xi}} - \int_D \boldsymbol{\nabla}\boldsymbol{u}(\boldsymbol{\xi}) : \mathbf{C} : \boldsymbol{\nabla}\boldsymbol{u}(\boldsymbol{\xi})\, dV_{\boldsymbol{\xi}}, \\
\int_D [\boldsymbol{v}(\boldsymbol{\xi}) \cdot \boldsymbol{L}\boldsymbol{u}(\boldsymbol{\xi}) - \boldsymbol{u}(\boldsymbol{\xi}) \cdot \boldsymbol{L}\boldsymbol{v}(\boldsymbol{\xi})]\, dV_{\boldsymbol{\xi}} &= \int_{\partial D} [\boldsymbol{v}(\boldsymbol{\xi}) \cdot \boldsymbol{t}(\boldsymbol{\xi};\boldsymbol{u}) - \boldsymbol{u}(\boldsymbol{\xi}) \cdot \boldsymbol{t}(\boldsymbol{\xi};\boldsymbol{v})]\, dS_{\boldsymbol{\xi}},
\end{aligned} \tag{3.4}$$

where $\boldsymbol{t}(\boldsymbol{\xi};\boldsymbol{u})$ is given by (2.3), and $\boldsymbol{L}$ is the Lamé operator as examined before.

To formulate the counterpart of (3.1) in terms of an alternative near-field operator that entails integration over the receiver surface, it is essential to show that the scattered tensor (2.8) is symmetric. This result is established next.

THEOREM 3.1 (Reciprocity). *For the scattering by a cavity, the following symmetry holds*

$$\widetilde{\boldsymbol{U}}(\boldsymbol{\xi},\boldsymbol{x}) = \left[\widetilde{\boldsymbol{U}}(\boldsymbol{x},\boldsymbol{\xi})\right]^{\mathrm{T}}, \quad \boldsymbol{x},\boldsymbol{\xi} \in \Omega^-. \tag{3.5}$$

Proof. Let $\tilde{\boldsymbol{u}}^k(\boldsymbol{\zeta},\boldsymbol{x})$ and $\tilde{\boldsymbol{u}}^j(\boldsymbol{\zeta},\boldsymbol{\xi})$ be the scattered fields at $\boldsymbol{\zeta} \in \Omega^-$ due to point sources acting respectively at $\boldsymbol{x} \in \Omega^-$ in the kth coordinate direction and at $\boldsymbol{\xi} \in \Omega^-$ in

the jth coordinate direction. On the basis of the Betti's third formula (3.4c), homogeneous Navier equation for the exterior domain Ω^- and radiation condition (2.6), it can be shown that

$$\int_\Gamma \left[\tilde{\boldsymbol{u}}^j(\boldsymbol{\zeta},\boldsymbol{\xi})\cdot\tilde{\boldsymbol{t}}^k(\boldsymbol{\zeta},\boldsymbol{x}) - \tilde{\boldsymbol{u}}^k(\boldsymbol{\zeta},\boldsymbol{x})\cdot\tilde{\boldsymbol{t}}^j(\boldsymbol{\zeta},\boldsymbol{\xi})\right] dS_{\boldsymbol{\zeta}} = 0, \quad \boldsymbol{x},\boldsymbol{\xi}\in\Omega^-. \tag{3.6}$$

Similarly, application of the Betti's third formula and homogeneous Navier equation to the Green's functions $\hat{\boldsymbol{u}}^k(\boldsymbol{\zeta},\boldsymbol{x})$ and $\hat{\boldsymbol{u}}^j(\boldsymbol{\zeta},\boldsymbol{\xi})$ over the interior domain Ω_{C} yields the identity

$$\int_\Gamma \left[\hat{\boldsymbol{u}}^j(\boldsymbol{\zeta},\boldsymbol{\xi})\cdot\hat{\boldsymbol{t}}^k(\boldsymbol{\zeta},\boldsymbol{x}) - \hat{\boldsymbol{u}}^k(\boldsymbol{\zeta},\boldsymbol{x})\cdot\hat{\boldsymbol{t}}^j(\boldsymbol{\zeta},\boldsymbol{\xi})\right] dS_{\boldsymbol{\zeta}} = 0, \quad \boldsymbol{x},\boldsymbol{\xi}\in\Omega^-. \tag{3.7}$$

For $\boldsymbol{x},\boldsymbol{\xi}\in\Omega^-$, one can write boundary integral representations

$$\begin{aligned}
\tilde{u}^k_j(\boldsymbol{\xi},\boldsymbol{x}) &= \int_\Gamma \left[\hat{\boldsymbol{u}}^j(\boldsymbol{\zeta},\boldsymbol{\xi})\cdot\tilde{\boldsymbol{t}}^k(\boldsymbol{\zeta},\boldsymbol{x}) - \hat{\boldsymbol{t}}^j(\boldsymbol{\zeta},\boldsymbol{\xi})\cdot\tilde{\boldsymbol{u}}^k(\boldsymbol{\zeta},\boldsymbol{x})\right] dS_{\boldsymbol{\zeta}},\\
\tilde{u}^j_k(\boldsymbol{x},\boldsymbol{\xi}) &= \int_\Gamma \left[\hat{\boldsymbol{u}}^k(\boldsymbol{\zeta},\boldsymbol{x})\cdot\tilde{\boldsymbol{t}}^j(\boldsymbol{\zeta},\boldsymbol{\xi}) - \hat{\boldsymbol{t}}^k(\boldsymbol{\zeta},\boldsymbol{x})\cdot\tilde{\boldsymbol{u}}^j(\boldsymbol{\zeta},\boldsymbol{\xi})\right] dS_{\boldsymbol{\zeta}}, \quad \boldsymbol{x},\boldsymbol{\xi}\in\Omega^-.
\end{aligned} \tag{3.8}$$

of the scattered field (e.g. [3]). On subtracting (3.8b) from the sum of (3.6), (3.7) and (3.8a), one finds that

$$\tilde{u}^k_j(\boldsymbol{\xi},\boldsymbol{x}) - \tilde{u}^j_k(\boldsymbol{x},\boldsymbol{\xi}) = \int_\Gamma \left[\boldsymbol{u}^j(\boldsymbol{\zeta},\boldsymbol{\xi})\cdot\boldsymbol{t}^k(\boldsymbol{\zeta},\boldsymbol{x}) - \boldsymbol{u}^k(\boldsymbol{\zeta},\boldsymbol{x})\cdot\boldsymbol{t}^j(\boldsymbol{\zeta},\boldsymbol{\xi})\right] dS_{\boldsymbol{\zeta}}, \tag{3.9}$$

where $\boldsymbol{u}^j = \hat{\boldsymbol{u}}^j + \tilde{\boldsymbol{u}}^j$ and $\boldsymbol{t}^j = \hat{\boldsymbol{t}}^j + \tilde{\boldsymbol{t}}^j$ denote respectively the *total* displacement and traction vectors at $\boldsymbol{\zeta}\in\Gamma$ due to a point source acting at $\boldsymbol{\xi}\in\Omega^-$ in the jth coordinate direction ($j=1,2,3$). By virtue of (2.5), the latter quantity vanishes identically on Γ which through (2.8) concludes the proof. □

One of the key steps in establishing the rationale for (3.1) is the proof that (3.2) represents a scattered field in Ω^-. The following theorem and its lemma aim to establish an analogous result for the sought "source-friendly" reformulation of (3.1).

THEOREM 3.2. *Let $\Gamma_2\subset\Sigma$ be a surface of limited extent and $\boldsymbol{h}\in L_2(\Gamma_2)$. Then a single-layer potential*

$$\boldsymbol{v}(\boldsymbol{\xi}) = \int_{\Gamma_2}\left[\widehat{\boldsymbol{U}}(\boldsymbol{x},\boldsymbol{\xi})\right]^{\mathrm{T}}\cdot\,\boldsymbol{h}(\boldsymbol{x})\,dS_{\boldsymbol{x}} = \int_{\Gamma_2}\hat{\boldsymbol{u}}^k(\boldsymbol{\xi},\boldsymbol{x})\,h_k(\boldsymbol{x})\,dS_{\boldsymbol{x}}, \quad \boldsymbol{\xi}\in\Omega\setminus\Gamma_2 \tag{3.10}$$

is a radiating solution to the homogeneous Navier equation in $\Omega\setminus\Gamma_2$, i.e.

$$\boldsymbol{L}\boldsymbol{v}(\boldsymbol{\xi}) + \rho\omega^2\boldsymbol{v}(\boldsymbol{\xi}) = \boldsymbol{0}, \quad \boldsymbol{\xi}\in\Omega\setminus\Gamma_2, \tag{3.11}$$

and

$$\lim_{R\to\infty}\int_{\Gamma_R}\left\{\hat{\boldsymbol{u}}^j(\boldsymbol{\xi},\boldsymbol{x})\cdot\boldsymbol{t}(\boldsymbol{\xi};\boldsymbol{v}) - \hat{\boldsymbol{t}}^j(\boldsymbol{\xi},\boldsymbol{x})\cdot\boldsymbol{v}(\boldsymbol{\xi})\right\}dS_{\boldsymbol{\xi}} = 0, \quad \boldsymbol{x}\in\Omega_R, \tag{3.12}$$

where $j=1,2,3$ and $\boldsymbol{t}(\boldsymbol{\xi};\boldsymbol{v}) = \boldsymbol{n}(\boldsymbol{\xi})\cdot\mathbf{C}:\boldsymbol{\nabla}\boldsymbol{v}(\boldsymbol{\xi})$ is the traction vector associated with the displacement field $\boldsymbol{v}$ on any regular surface in Ω with unit normal $\boldsymbol{n}$.

Proof. For $\boldsymbol{x}\in\Gamma_2$ and $\boldsymbol{\xi}\in\Omega\setminus\Gamma_2$, $\widehat{\boldsymbol{U}}(\boldsymbol{\xi},\boldsymbol{x})$ is regular and (3.10) accordingly permits differentiation under the integral sign. With such result, (3.11) follows directly from

the fact that $\hat{\boldsymbol{u}}^k$ $(k=1,2,3)$ satisfies the homogeneous Navier equation away from the surface Γ_2. On the basis of (2.3) and (3.10), on the other hand, one finds that

$$\int_{\Gamma_R} \left\{ \hat{\boldsymbol{u}}^j(\boldsymbol{\xi},\boldsymbol{x}) \cdot \boldsymbol{t}(\boldsymbol{\xi};\boldsymbol{v}) - \hat{\boldsymbol{t}}^j(\boldsymbol{\xi},\boldsymbol{x}) \cdot \boldsymbol{v}(\boldsymbol{\xi}) \right\} dS_{\boldsymbol{\xi}} =$$
$$\int_{\Gamma_2} g_k(\boldsymbol{x}) \int_{\Gamma_R} \left\{ \hat{\boldsymbol{t}}^k(\boldsymbol{\xi},\boldsymbol{y}) \cdot \hat{\boldsymbol{u}}^j(\boldsymbol{\xi},\boldsymbol{x}) - \hat{\boldsymbol{t}}^j(\boldsymbol{\xi},\boldsymbol{x}) \cdot \hat{\boldsymbol{u}}^k(\boldsymbol{\xi},\boldsymbol{y}) \right\} \, \mathrm{d}S_{\boldsymbol{\xi}} \, dS_{\boldsymbol{x}}. \tag{3.13}$$

on any regular surface in Ω with unit normal $\boldsymbol{n}$. By virtue of (3.13), statement (3.12) immediately follows from the fact that the half-space displacement Green's function $\hat{\boldsymbol{u}}^k(\cdot,\boldsymbol{z})$ $(k=1,2,3)$ is a radiating solution to the homogeneous Navier equation in $\Omega\backslash\{\boldsymbol{z}\}$, see [16]. □

LEMMA 3.3.

For a given "source function" $\boldsymbol{h} \in L_2(\Gamma_2)$, radiating solution to the scattering problem for a cavity Ω_C in the half-space Ω illuminated by the free field

$$\mathring{\boldsymbol{v}}(\boldsymbol{x}) = \int_{\Gamma_2} \left[\widehat{\boldsymbol{U}}(\boldsymbol{\xi},\boldsymbol{x}) \right]^{\mathrm{T}} \cdot \boldsymbol{h}(\boldsymbol{\xi}) \, dS_{\boldsymbol{\xi}}, \quad \boldsymbol{x} \in \Omega, \tag{3.14}$$

is given by the scattered field

$$\tilde{\boldsymbol{v}}(\boldsymbol{x}) = \int_{\Gamma_2} \left[\widetilde{\boldsymbol{U}}(\boldsymbol{\xi},\boldsymbol{x}) \right]^{\mathrm{T}} \cdot \boldsymbol{h}(\boldsymbol{\xi}) \, dS_{\boldsymbol{\xi}}, \quad \boldsymbol{x} \in \Omega^-, \tag{3.15}$$

where $\widehat{\boldsymbol{U}}$ and $\widetilde{\boldsymbol{U}}$ are given respectively by (2.7) and (2.8).

Proof. With the aid of (2.8) and reciprocity statement (3.5), (3.15) can be rewritten as

$$\tilde{\boldsymbol{v}}(\boldsymbol{x}) = \int_{\Gamma_2} \tilde{\boldsymbol{u}}^k(\boldsymbol{x},\boldsymbol{\xi}) \, h_k(\boldsymbol{\xi}) \, dS_{\boldsymbol{\xi}}, \quad \boldsymbol{x} \in \Omega^-. \tag{3.16}$$

By virtue of (2.5), integral representation of the scattered field $\tilde{\boldsymbol{u}}^k$ [30] in terms of the total displacement field $\boldsymbol{u}^k$ over the cavity boundary Γ can be expressed as

$$\tilde{\boldsymbol{u}}^k(\boldsymbol{x},\boldsymbol{\xi}) = -\int_{\Gamma} \hat{\boldsymbol{t}}^j(\boldsymbol{\eta},\boldsymbol{x}) \, u_j^k(\boldsymbol{\eta},\boldsymbol{\xi}) \, dS_{\boldsymbol{\eta}}, \quad \boldsymbol{x} \in \Omega^-, \quad \boldsymbol{\xi} \in \Gamma_2. \tag{3.17}$$

By use of (3.17) in (3.16) and interchanging order of integration, one finds

$$\tilde{\boldsymbol{v}}(\boldsymbol{x}) = -\int_{\Gamma} \hat{\boldsymbol{t}}^j(\boldsymbol{\eta},\boldsymbol{x}) \, v_j(\boldsymbol{\eta}) \, dS_{\boldsymbol{\eta}}, \quad \boldsymbol{x} \in \Omega^-, \tag{3.18}$$

where

$$\boldsymbol{v}(\boldsymbol{x}) = \int_{\Gamma_2} \boldsymbol{u}^k(\boldsymbol{x},\boldsymbol{\xi}) \, h_k(\boldsymbol{\xi}) \, dS_{\boldsymbol{\xi}}, \quad \boldsymbol{x} \in \Omega^-, \tag{3.19}$$

It is seen from (3.18) that $\tilde{\boldsymbol{v}}(\boldsymbol{x})$ admits a representation similar to (3.17) in terms of a double-layer potential. Since $\boldsymbol{x} \in \Omega^-$, it can be shown using the radiating property of $\hat{\boldsymbol{u}}^k$ that the right-hand side of (3.18) is itself a *radiating* solution of the homogeneous Navier equation in Ω^- so that

$$\boldsymbol{L}\tilde{\boldsymbol{v}}^k(\boldsymbol{x}) + \rho\omega^2 \tilde{\boldsymbol{v}}^k(\boldsymbol{x}) = \boldsymbol{0}, \quad \boldsymbol{x} \in \Omega^-,$$
$$\lim_{R\to\infty} \int_{\Gamma_R} \left\{ \hat{\boldsymbol{u}}^j(\boldsymbol{\xi},\boldsymbol{x}) \cdot \boldsymbol{t}(\boldsymbol{\xi};\tilde{\boldsymbol{v}}) - \hat{\boldsymbol{t}}^j(\boldsymbol{\xi},\boldsymbol{x}) \cdot \tilde{\boldsymbol{v}}(\boldsymbol{\xi}) \right\} dS_{\boldsymbol{\xi}} = 0, \quad \boldsymbol{x} \in \Omega_R^-, \tag{3.20}$$

On applying (2.3) to (3.14) and (3.16) and interchanging the order of integral and differential operators, one finds from (2.1), (2.3) and (2.5) that

$$\boldsymbol{t}(\boldsymbol{y};\tilde{\boldsymbol{v}}) \;=\; \int_{\Gamma_2} \tilde{\boldsymbol{t}}^k(\boldsymbol{y},\boldsymbol{\xi})\, h_k(\boldsymbol{\xi})\, dS_{\boldsymbol{\xi}} \;=\; \begin{cases} \boldsymbol{0}, & \boldsymbol{y}\in\Sigma, \\ -\boldsymbol{t}(\boldsymbol{y};\mathring{\boldsymbol{v}}), & \boldsymbol{y}\in\Gamma, \end{cases} \tag{3.21}$$

in the limits as $\boldsymbol{x}\to\boldsymbol{y}\in\Sigma$ and $\boldsymbol{x}\to\boldsymbol{y}\in\Gamma$, respectively. Given the fact that $\Gamma=\partial\Omega_{\rm C}$ and $\Omega^- = \Omega\setminus(\Omega_{\rm C}\cup\Gamma)$, equations (3.20) and (3.21) indeed demonstrate that $\tilde{\boldsymbol{v}}$ is a radiating solution to the scattering problem for a cavity $\Omega_{\rm C}$ illuminated by the free field (3.14). □

4. Adjoint formulation of the linear sampling method. With the foregoing developments, linear sampling equation (3.1) aiding the full waveform tomography of a semi-infinite elastic solid can now be reformulated so that the featured integration is performed over the receiver surface Γ_2 in lieu of Γ_1. To this end, let the sampling point $\boldsymbol{z}\in\Omega$ be fixed. The idea is to establish an alternative near-field operator $\boldsymbol{G}\colon L_2(\Gamma_2)\to L_2(\Gamma_1)$ that synthesizes experimental observations in terms of the scattered tensor $\widetilde{\boldsymbol{U}}$, and to seek the vector density $\boldsymbol{h}_{\boldsymbol{z},\boldsymbol{d}}(\cdot)\equiv\boldsymbol{h}(\cdot;\boldsymbol{z},\boldsymbol{d})\in L_2(\Gamma_2)$ as a solution to the integral equation of the first kind

$$(\boldsymbol{G}\boldsymbol{h}_{\boldsymbol{z},\boldsymbol{d}})(\boldsymbol{x}) = \widehat{\boldsymbol{U}}(\boldsymbol{x},\boldsymbol{z})\cdot\boldsymbol{d}, \quad \boldsymbol{x}\in\Gamma_1, \quad \boldsymbol{z}\in\Omega. \tag{4.1}$$

Adopting fundamental hypotheses of the linear sampling method, $\boldsymbol{G}$ must be designed so that

- for $\boldsymbol{z}\in\Omega_{\rm C}$, there exists a *unique* solution $\boldsymbol{h}_{\boldsymbol{z},\boldsymbol{d}}$ to equation (4.1) such that $\lim_{\boldsymbol{z}\to\boldsymbol{y}\in\Gamma}\|\boldsymbol{h}_{\boldsymbol{z},\boldsymbol{d}}\|_{L_2(\Gamma_2)}=\infty$;
- for $\boldsymbol{z}\in\Omega\setminus(\Omega_{\rm C}\cup\Gamma)$, there exists an *approximate* solution $\boldsymbol{h}^\tau_{\boldsymbol{z},\boldsymbol{d}}$ to (4.1) such that $\lim_{\tau\to0}\|\boldsymbol{h}^\tau_{\boldsymbol{z},\boldsymbol{d}}\|_{L_2(\Gamma_2)}=\infty$ where τ is the approximation parameter. With reference to Fig. 4.1, an approximate solution $\boldsymbol{h}^\tau_{\boldsymbol{z},\boldsymbol{d}}$ is in this study understood in the sense of a perturbed scatterer domain (see also [29]).

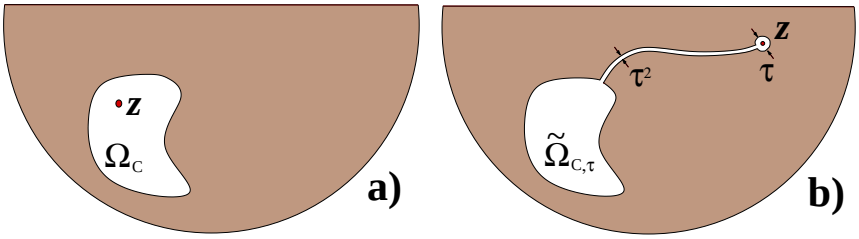

FIG. 4.1. *Sampling cases: a)* $\boldsymbol{z}\in\Omega_C$*, "true" obstacle; b)* $\boldsymbol{z}\in\Omega\setminus\overline{\Omega}_C$*, perturbed obstacle.*

With such prerequisites, the *unboundedness* property of the sought vector density $\boldsymbol{h}_{\boldsymbol{z},\boldsymbol{d}}$ can then be used to reconstruct a hidden cavity $\Omega_{\rm C}$ by sampling the region of interest within Ω through an array of sampling points $\boldsymbol{z}$ and identifying $\Omega_{\rm C}$ through an assembly of sampling points where $\|\boldsymbol{h}_{\boldsymbol{z},\boldsymbol{d}}\|_{L_2(\Gamma_2)}$ is bounded. As elucidated earlier, such identification procedure would make sense even when the density of source points on Γ_1, used to illuminate the cavity, is limited.

To facilitate the ensuing developments, it is useful to make reference to the near-field operator $\boldsymbol{F}$ in (3.2) and introduce its adjoint counterpart $\boldsymbol{F}^*\colon L_2(\Gamma_2)\to L_2(\Gamma_1)$ by the ensuing proposition:

LEMMA 4.1. *For all* $\boldsymbol{g}\in L_2(\Gamma_1)$ *and* $\boldsymbol{e}\in L_2(\Gamma_2)$,

$$(\boldsymbol{F}\boldsymbol{g},\boldsymbol{e})_{L_2(\Gamma_2)} = (\boldsymbol{g},\boldsymbol{F}^*\boldsymbol{e})_{L_2(\Gamma_1)}, \tag{4.2}$$

where $\boldsymbol{F}$ *is defined by (3.2), and*

$$(\boldsymbol{F}^*\boldsymbol{e})(\boldsymbol{x}) := \int_{\Gamma_2} \overline{\left[\widetilde{\boldsymbol{U}}(\boldsymbol{\xi},\boldsymbol{x})\right]}^{\mathrm{T}} \cdot \boldsymbol{e}(\boldsymbol{\xi})\, dS_{\boldsymbol{\xi}}, \quad \boldsymbol{x}\in\Gamma_1. \tag{4.3}$$

with overbar denoting complex conjugation.

Proof. The statement of the lemma in terms of (4.2) and (4.3) can be established using (3.2), (3.3), and interchanging the order of integration. □

To arrive at a form of $\boldsymbol{G}$ that yields the required solvability and unboundedness properties in terms of $\boldsymbol{h}_{\boldsymbol{z},\boldsymbol{d}}$, one is tempted to employ the result of Lemma 4.1 and postulate the integral equation

$$\int_{\Gamma_2} \overline{\left[\widetilde{\boldsymbol{U}}(\boldsymbol{\xi},\boldsymbol{x})\right]}^{\mathrm{T}} \cdot \boldsymbol{e}(\boldsymbol{\xi})\, dS_{\boldsymbol{\xi}} = \overline{\left[\widehat{\boldsymbol{U}}(\boldsymbol{z},\boldsymbol{x})\right]}^{\mathrm{T}} \cdot \boldsymbol{d}, \quad \boldsymbol{x}\in\Gamma_1, \quad \boldsymbol{z}\in\Omega, \tag{4.4}$$

as a basis for the "source-friendly"alternative to (3.1). On employing the symmetry of the elastodynamic half-space displacement Green's tensor (2.7) and letting $\boldsymbol{h}=\overline{\boldsymbol{e}}$, integral equation (4.4) can be recast in the form of (4.1) with

$$(\boldsymbol{G}\boldsymbol{h}_{\boldsymbol{z},\boldsymbol{d}})(\boldsymbol{x}) := \int_{\Gamma_2} \left[\widetilde{\boldsymbol{U}}(\boldsymbol{\xi},\boldsymbol{x})\right]^{\mathrm{T}} \cdot \boldsymbol{h}_{\boldsymbol{z},\boldsymbol{d}}(\boldsymbol{\xi})\, dS_{\boldsymbol{\xi}}, \quad \boldsymbol{x}\in\Gamma_1. \tag{4.5}$$

With reference to Lemma 3.3, the conjugation of (4.4) represents a key step that establishes the near-field operator (4.5) as a *radiating* elastodynamic field in the sense of (2.6) and thus enables a direct use of the results introduced in Section 3. It is also useful to note that for $\widetilde{\boldsymbol{U}}\in L_2(\Gamma_2\times\Gamma_1)$, the near-field operator $\boldsymbol{G}$ is well-defined, linear, and bounded from $L_2(\Gamma_2)$ into $L_2(\Gamma_1)$. The latter property can be demonstrated via the Cauchy-Schwarz inequality

$$\|\boldsymbol{G}\boldsymbol{h}\|^2_{L_2(\Gamma_1)} \le \|\boldsymbol{h}\|^2_{L_2(\Gamma_2)} \left(\sum_{k=1}^{3}\sum_{j=1}^{3}\int_{\Gamma_1}\int_{\Gamma_2} \left|\tilde{u}_j^k(\boldsymbol{\xi},\boldsymbol{x})\right|^2 dS_{\boldsymbol{x}}\, dS_{\boldsymbol{\xi}}\right) \tag{4.6}$$

where $|\cdot|$ denotes the complex modulus. One may also show [22] that the linear integral operator $\boldsymbol{G}$ is *compact* from $L_2(\Gamma_2)$ into $L_2(\Gamma_1)$, thus rendering the linear equation (4.1) ill-posed.

5. Mathematical basis. To validate the proposed developments, it is first necessary to establish the existence and uniqueness theorems for the integral equation of the first kind given by (4.1) and (4.5). Assuming the approach taken in [29], case $\boldsymbol{z}\in\Omega_c$ is considered first, followed by the analysis for $\boldsymbol{z}\in\Omega^-$. As mentioned earlier, it is assumed that a unique solution $\tilde{\boldsymbol{u}}^k\in H^1_{loc}(\Omega^-)$ to the forward scattering problem (2.4)-(2.6) exists.

THEOREM 5.1 (Solvability). *Let* $\boldsymbol{z}\in\Omega_C$ *be fixed, and let* Ω_C *be a cavity. Then the equation*

$$(\boldsymbol{G}\boldsymbol{h}_{\boldsymbol{z},\boldsymbol{d}})(\boldsymbol{x}) = \widehat{\boldsymbol{U}}(\boldsymbol{x},\boldsymbol{z})\cdot\boldsymbol{d}, \quad \boldsymbol{x}\in\Gamma_1, \quad \boldsymbol{z}\in\Omega_C, \tag{5.1}$$

where $\boldsymbol{G}$ is given by (4.5), possesses a solution $\boldsymbol{h}_{\boldsymbol{z},\boldsymbol{d}} \in L_2(\Gamma_2)$ if and only if there exists an elastodynamic solution $\mathring{\boldsymbol{v}}$ to the interior Neumann problem

$$\begin{aligned} \boldsymbol{L}\mathring{\boldsymbol{v}}(\boldsymbol{x}) + \rho\,\omega^2 \mathring{\boldsymbol{v}}(\boldsymbol{x}) &= \boldsymbol{0}, \quad \boldsymbol{x}\in\Omega_C, \\ \boldsymbol{t}(\boldsymbol{x};\mathring{\boldsymbol{v}}) + \widehat{\boldsymbol{T}}(\boldsymbol{x},\boldsymbol{z})\cdot\boldsymbol{d} &= \boldsymbol{0}, \quad \boldsymbol{x}\in\Gamma, \end{aligned} \tag{5.2}$$

that is expressible in the form of (3.14).

Proof. Let $\boldsymbol{h}_{\boldsymbol{z},\boldsymbol{d}} \in L_2(\Gamma_2)$ be a solution to (5.1) and define $\mathring{\boldsymbol{v}}$ according to (3.14) through

$$\mathring{\boldsymbol{v}}(\boldsymbol{x}) = \int_{\Gamma_2} \left[\widehat{\boldsymbol{U}}(\boldsymbol{\xi},\boldsymbol{x})\right]^{\mathrm{T}} \cdot \boldsymbol{h}(\boldsymbol{\xi})\, dS_{\boldsymbol{\xi}}, \quad \boldsymbol{x}\in\Omega. \tag{5.3}$$

Since $\Gamma_2 \cap \Omega_{\mathrm{C}} = \emptyset$, it can be shown using differentiation under the integral sign that $\mathring{\boldsymbol{v}}(\boldsymbol{x})$ satisfies the homogeneous Navier equation (5.2a) for $\boldsymbol{x} \in \Omega_{\mathrm{C}} \subset \Omega \setminus \Gamma_2$. On the other hand, from Lemma 3.3, the associated scattered field

$$\tilde{\boldsymbol{v}}(\boldsymbol{x}) = \int_{\Gamma_2} \left[\widetilde{\boldsymbol{U}}(\boldsymbol{\xi},\boldsymbol{x})\right]^{\mathrm{T}} \cdot \boldsymbol{h}(\boldsymbol{\xi})\, dS_{\boldsymbol{\xi}}, \quad \boldsymbol{x}\in\Omega^- \tag{5.4}$$

is a radiating solution to the homogeneous Navier equation in Ω^-. Since $\boldsymbol{z}\in\Omega_{\mathrm{C}}$, it follows that $\widehat{\boldsymbol{U}}(\boldsymbol{x},\boldsymbol{z})\cdot\boldsymbol{d}$, $\boldsymbol{x}\in\Omega^-$ is also a radiating solution to the homogeneous Navier equation in Ω^-, and, by use of (4.5) and (5.1), that $\tilde{\boldsymbol{v}}(\boldsymbol{x}) = \widehat{\boldsymbol{U}}(\boldsymbol{x},\boldsymbol{z})\cdot\boldsymbol{d}$ for $\boldsymbol{x}\in\Gamma_1$. With the aid of the Holmgren's uniqueness theorem [14], the latter equality can be extended throughout Ω^- so that

$$\tilde{\boldsymbol{v}}(\boldsymbol{x}) = \widehat{\boldsymbol{U}}(\boldsymbol{x},\boldsymbol{z})\cdot\boldsymbol{d}, \quad \boldsymbol{x}\in\Omega^-. \tag{5.5}$$

For the scattering by a cavity, one must have

$$\boldsymbol{t}(\boldsymbol{x};\mathring{\boldsymbol{v}}) + \boldsymbol{t}(\boldsymbol{x};\tilde{\boldsymbol{v}}) = \boldsymbol{0}, \quad \boldsymbol{x}\in\Gamma, \tag{5.6}$$

see also (3.21). From (2.3), (2.9) and (5.5), the traction vector $\boldsymbol{t}(\boldsymbol{x};\tilde{\boldsymbol{v}})$ on any surface strictly inside Ω^- is given by $\widehat{\boldsymbol{T}}(\boldsymbol{x},\boldsymbol{z})\cdot\boldsymbol{d}$, which, through (5.6) yields (5.2b) in the limit as $\boldsymbol{x}\to\boldsymbol{y}\in\Gamma$.

Conversely, let $\mathring{\boldsymbol{v}}(\boldsymbol{x})$ be given by (5.3) (same as (3.14)) and let it satisfy (5.2). With such hypotheses, one may take $\mathring{\boldsymbol{v}}$ as a free field for the scattering by a cavity Ω_{C}. From Lemma 3.3, the unique radiating solution to this scattering problem is given by (5.4) that satisfies the Neumann boundary condition (5.6). From (5.2b) and (5.6), one finds that

$$\boldsymbol{t}(\boldsymbol{x};\tilde{\boldsymbol{v}}) = \widehat{\boldsymbol{T}}(\boldsymbol{x},\boldsymbol{z})\cdot\boldsymbol{d}, \quad \boldsymbol{x}\in\Gamma. \tag{5.7}$$

By virtue of the Holmgren's uniqueness theorem, (5.7) can be used to obtain (5.5) which yields (5.1) in the limit as $\boldsymbol{x}\to\boldsymbol{y}\in\Gamma_1$. □

5.1. Approximation property of single-layer potentials. Having reduced the issue of solvability of (4.1) with $\boldsymbol{G}$ given by (4.5) to the solution of interior Neumann problem (5.2) in the form of (3.14), it is next necessary to establish the denseness property of the latter potential representation.

To facilitate the ensuing developments, let $D \subset \Omega$ be a bounded domain with boundary ∂D of class $C^{1,\alpha}$, and let $L_2(D)$ be a Hilbert space of square-integrable vector fields with the standard inner product

$$(\boldsymbol{v},\boldsymbol{u})_{L_2(D)} = \int_D \overline{\boldsymbol{v}}(\boldsymbol{\xi})\cdot\boldsymbol{u}(\boldsymbol{\xi})\, dV_{\boldsymbol{\xi}}. \tag{5.8}$$

Similarly, one may introduce $H^1(D) = \{\boldsymbol{u}\in L_2(D), \boldsymbol{\nabla u}\in L_2(D)\}$ as a Hilbert space equipped with the Hermitian inner product

$$(\boldsymbol{v},\boldsymbol{u})_{H^1(D)} = \theta\int_D \overline{\boldsymbol{v}}(\boldsymbol{\xi})\cdot\boldsymbol{u}(\boldsymbol{\xi})\,dV_{\boldsymbol{\xi}} + \int_D \boldsymbol{\nabla}\overline{\boldsymbol{v}}(\boldsymbol{\xi}):\mathbf{C}:\boldsymbol{\nabla u}(\boldsymbol{\xi})\,dV_{\boldsymbol{\xi}}, \tag{5.9}$$

where $\mathbb{R}\ni\theta>0$. With such definitions, let $\mathbb{H}(D)$ be a set of classical solutions to the homogeneous Navier equation

$$\mathbb{H}(D) = \big\{\boldsymbol{u}\in C^2(D)\cap C^1(\overline{D}) : \boldsymbol{Lu}+\rho\omega^2\boldsymbol{u}=\boldsymbol{0} \ \text{ in } D\big\},$$

whose closure, $\overline{\mathbb{H}(D)}$, is defined with respect to the norm

$$\|\boldsymbol{u}\|_{H^1(D)} = \sqrt{(\boldsymbol{u},\boldsymbol{u})_{H^1(D)}}. \tag{5.10}$$

Next, consider the single-layer integral operator $\boldsymbol{S}: L_2(\Gamma_2)\to\overline{\mathbb{H}(D)}$ given by

$$(\boldsymbol{Sh})(\boldsymbol{\xi}) := \int_{\Gamma_2}\Big[\widehat{\boldsymbol{U}}(\boldsymbol{x},\boldsymbol{\xi})\Big]^{\mathrm{T}}\cdot\boldsymbol{h}(\boldsymbol{x})\,dS_{\boldsymbol{x}}, \quad \boldsymbol{\xi}\in D. \tag{5.11}$$

For $\Gamma_2\cap\overline{D}=\emptyset$, assumed in this study, $\boldsymbol{Sh}\in C^\infty\left(\overline{D}\right)\subset\{C^2(D)\cap C^1(\overline{D})\}$. By virtue of this result and the fact that $\boldsymbol{Sh}$ satisfies the homogeneous Navier equation in D according to Theorem 3.2, it immediately follows that $\boldsymbol{Sh}\in\mathbb{H}(D)$.

LEMMA 5.2. *For all $\boldsymbol{h}\in L_2(\Gamma_2)$ and $\boldsymbol{u}\in\overline{\mathbb{H}(D)}$, the following identity holds*

$$(\boldsymbol{Sh},\boldsymbol{u})_{L_2(D)} = (\boldsymbol{h},\boldsymbol{S}_D^*\boldsymbol{u})_{L_2(\Gamma_2)}, \tag{5.12}$$

where $\boldsymbol{S}_D^*:\overline{\mathbb{H}(D)}\to L_2(\Gamma_2)$ is given by

$$(\boldsymbol{S}_D^*\boldsymbol{u})(\boldsymbol{x}) := \int_D\Big[\overline{\widehat{\boldsymbol{U}}(\boldsymbol{\xi},\boldsymbol{x})}\Big]^{\mathrm{T}}\cdot\boldsymbol{u}(\boldsymbol{\xi})\,dV_{\boldsymbol{\xi}}, \quad \boldsymbol{x}\in\Gamma_2.$$

Proof. For $\boldsymbol{h}\in L_2(\Gamma_2)$ and $\boldsymbol{u}\in\mathbb{H}(D)$,

$$\begin{aligned}(\boldsymbol{Sh},\boldsymbol{u})_{L_2(D)} &= \int_D\left\{\int_{\Gamma_2}\Big[\overline{\widehat{\boldsymbol{U}}(\boldsymbol{x},\boldsymbol{\xi})}\Big]^{\mathrm{T}}\cdot\overline{\boldsymbol{h}(\boldsymbol{x})}\,dS_{\boldsymbol{x}}\right\}\cdot\boldsymbol{u}(\boldsymbol{\xi})\,dV_{\boldsymbol{\xi}}\\ &= \int_{\Gamma_2}\overline{\boldsymbol{h}(\boldsymbol{x})}\cdot\left\{\int_D\overline{\widehat{\boldsymbol{U}}(\boldsymbol{x},\boldsymbol{\xi})}\cdot\boldsymbol{u}(\boldsymbol{\xi})\,dV_{\boldsymbol{\xi}}\right\}dS_{\boldsymbol{x}}.\end{aligned} \tag{5.13}$$

The claim of the lemma now follows by virtue of the symmetry property $\widehat{\boldsymbol{U}}(\boldsymbol{x},\boldsymbol{\xi}) = \Big[\widehat{\boldsymbol{U}}(\boldsymbol{\xi},\boldsymbol{x})\Big]^{\mathrm{T}}$ and the fact that $\mathbb{H}(D)$ is dense in $\overline{\mathbb{H}(D)}$. ∎

LEMMA 5.3. *For all $\boldsymbol{h}\in L_2(\Gamma_2)$ and $\boldsymbol{u}\in\overline{\mathbb{H}(D)}$, one has*

$$(\boldsymbol{Sh},\boldsymbol{u})_{H^1(D)} = (\boldsymbol{h},\boldsymbol{S}^*\boldsymbol{u})_{L_2(\Gamma_2)}, \tag{5.14}$$

where $\boldsymbol{S}^*:\overline{\mathbb{H}(D)}\to L_2(\Gamma_2)$ admits the representation

$$(\boldsymbol{S}^*\boldsymbol{u})(\boldsymbol{x}) := \big(\theta+\rho\omega^2\big)\int_D\Big[\overline{\widehat{\boldsymbol{U}}(\boldsymbol{\xi},\boldsymbol{x})}\Big]^{\mathrm{T}}\cdot\boldsymbol{u}(\boldsymbol{\xi})\,dV_{\boldsymbol{\xi}} + \int_{\partial D}\Big[\overline{\widehat{\boldsymbol{U}}(\boldsymbol{\xi},\boldsymbol{x})}\Big]^{\mathrm{T}}\cdot\boldsymbol{t}(\boldsymbol{\xi};\boldsymbol{u})\,dS_{\boldsymbol{\xi}},$$
$$\boldsymbol{x}\in\Gamma_2, \quad \mathbb{R}\ni\theta>0 \tag{5.15}$$

with the traction vector $\boldsymbol{t} \in H^{-1/2}(\partial D)$ *understood in the sense of the trace of* $\boldsymbol{u} \in H^1(D)$ *[26].*

Proof. As demonstrated earlier, $\boldsymbol{Sh} \in \mathbb{H}(D)$ for $\boldsymbol{h} \in L_2(\Gamma_2)$. It can further be shown that whenever $\boldsymbol{Sh} \in \mathbb{H}(D)$, its complex conjugate belongs to the same space, i.e. $\overline{\boldsymbol{Sh}} \in \mathbb{H}(D)$. Now let $\boldsymbol{u} \in \mathbb{H}(D)$. By use of the Betti's first formula (3.4a), homogeneous Navier equation for the vector field $\boldsymbol{u}$ in D, and inner product (5.9), one finds

$$(\boldsymbol{Sh}, \boldsymbol{u})_{H^1(D)} = \left(\theta + \rho\omega^2\right) (\boldsymbol{Sh}, \boldsymbol{u})_{L_2(D)} + (\boldsymbol{Sh}, \boldsymbol{t}(\cdot; \boldsymbol{u}))_{L_2(\partial D)}. \tag{5.16}$$

Analogous to the proof of Lemma 5.2, relationship (5.14) can be obtained from (5.16) by employing the symmetry property of $\widehat{\boldsymbol{U}}$ and interchanging the order of integration. The statement of the lemma then follows by the denseness argument. ∎

On the basis of (5.15), one may introduce the vector field

$$\begin{aligned} \boldsymbol{v}(\boldsymbol{x}) &:= \overline{(\boldsymbol{S}^* \boldsymbol{u})}(\boldsymbol{x}) \\ &= \left(\theta + \rho\omega^2\right) \int_D \left[\widehat{\boldsymbol{U}}(\boldsymbol{\xi}, \boldsymbol{x})\right]^{\mathrm{T}} \cdot \overline{\boldsymbol{u}(\boldsymbol{\xi})}\, dV_{\boldsymbol{\xi}} + \int_{\partial D} \left[\widehat{\boldsymbol{U}}(\boldsymbol{\xi}, \boldsymbol{x})\right]^{\mathrm{T}} \cdot \overline{\boldsymbol{t}(\boldsymbol{\xi}; \boldsymbol{u})}\, dS_{\boldsymbol{\xi}}, \quad \boldsymbol{x} \in \Omega \setminus \partial D, \quad \boldsymbol{u} \in \overline{\mathbb{H}(D)}. \end{aligned} \tag{5.17}$$

By use of the Lax's theorem [22], it can be shown that the volume potential in (5.17) is a bounded linear operator from $L_2(D) \supset H^1(D)$ into $H^2_{loc}(\Omega)$. Accordingly, since the single-layer potential in (5.17) is a bounded linear operator from $H^{-1/2}(\partial D)$ into $H^1_{loc}(\Omega \setminus \overline{D})$ (see [24]), one can conclude that the mapping $\boldsymbol{u} \longmapsto \boldsymbol{v}$ given by (5.17) defines a bounded linear operator from $H^1(D)$ into $H^1_{loc}(\Omega \setminus \overline{D})$. Since elastic potentials behave near boundaries much like ordinary harmonic potentials, it can be shown that

$$\boldsymbol{v}(\boldsymbol{x}) = \boldsymbol{v}_+(\boldsymbol{x}) = \boldsymbol{v}_-(\boldsymbol{x}), \quad \boldsymbol{t}_+(\boldsymbol{x}; \boldsymbol{v}) - \boldsymbol{t}_-(\boldsymbol{x}; \boldsymbol{v}) = -\overline{\boldsymbol{t}(\boldsymbol{x}; \boldsymbol{u})}, \quad \boldsymbol{x} \in \partial D, \tag{5.18}$$

where

$$\boldsymbol{v}_\pm(\boldsymbol{x}) = \lim_{\varepsilon \to 0} \boldsymbol{v}(\boldsymbol{x} \pm \varepsilon \boldsymbol{n}), \quad \boldsymbol{t}_\pm(\boldsymbol{x}; \boldsymbol{v}) = \boldsymbol{n}(\boldsymbol{x}) \cdot \mathbf{C} : \{\lim_{\varepsilon \to 0} \boldsymbol{\nabla} \boldsymbol{v}(\boldsymbol{x} \pm \varepsilon \boldsymbol{n})\}, \quad \boldsymbol{x} \in \partial D$$

with $\boldsymbol{n}$ representing the unit outward normal to D.

For $\boldsymbol{x} \in D$, the right-hand side of (5.17) can be differentiated under the integral sign. Owing to the fact that

$$\boldsymbol{L}\hat{\boldsymbol{u}}^k(\boldsymbol{x}, \boldsymbol{\xi}) + \rho\omega^2 \hat{\boldsymbol{u}}^k(\boldsymbol{x}, \boldsymbol{\xi}) + \delta_{ki}\, \boldsymbol{\delta}(\boldsymbol{x} - \boldsymbol{\xi}) \boldsymbol{e}_i = \boldsymbol{0}, \quad \boldsymbol{x} \in D,$$

where δ_{ki} is the Kronecker delta, $\boldsymbol{\delta}(\boldsymbol{x} - \boldsymbol{\xi})$ is the Dirac delta function and $\boldsymbol{e}_i$ is a unit vector in the i-th coordinate direction, it can be shown that

$$\boldsymbol{L}\boldsymbol{v}(\boldsymbol{x}) + \rho\omega^2 \boldsymbol{v}(\boldsymbol{x}) = -\left(\theta + \rho\omega^2\right) \overline{\boldsymbol{u}(\boldsymbol{x})}, \quad \boldsymbol{x} \in D. \tag{5.19}$$

In what follows, it is assumed that $\boldsymbol{u} \in \mathbb{H}(D)$. By this assumption, the use of Betti's second formula (3.4b), (5.18) and (5.19), one finds

$$\begin{aligned} \|\boldsymbol{u}\|^2_{H^1(D)} &= \left(\theta + \rho\omega^2\right) \int_D \overline{\boldsymbol{u}(\boldsymbol{\xi})} \cdot \boldsymbol{u}(\boldsymbol{\xi})\, dV_{\boldsymbol{\xi}} + \int_{\partial D} \overline{\boldsymbol{u}(\boldsymbol{\xi})} \cdot \boldsymbol{t}(\boldsymbol{\xi}; \boldsymbol{u})\, dS_{\boldsymbol{\xi}} \\ &= -\int_D \overline{\boldsymbol{u}}(\boldsymbol{\xi}) \cdot \left[\boldsymbol{L}\overline{\boldsymbol{v}}(\boldsymbol{\xi}) + \rho\omega^2 \overline{\boldsymbol{v}}(\boldsymbol{\xi})\right] dV_{\boldsymbol{\xi}} \\ &\quad -\int_{\partial D} \overline{\boldsymbol{u}}(\boldsymbol{\xi}) \cdot \left[\boldsymbol{t}_+(\boldsymbol{\xi}; \overline{\boldsymbol{v}}) - \boldsymbol{t}_-(\boldsymbol{\xi}; \overline{\boldsymbol{v}})\right] dS_{\boldsymbol{\xi}} \end{aligned} \tag{5.20}$$

LEMMA 5.4. *For all* $\boldsymbol{u}\in\overline{\mathbb{H}(D)}$,

$$\|\boldsymbol{u}\|^2_{H^1(D)}=\int_{\partial D}\left[\boldsymbol{v}(\boldsymbol{\xi})\cdot\boldsymbol{t}(\boldsymbol{\xi};\boldsymbol{u})-\boldsymbol{u}(\boldsymbol{\xi})\cdot\boldsymbol{t}_+(\boldsymbol{\xi};\boldsymbol{v})\right]dS_{\boldsymbol{\xi}}, \tag{5.21}$$

where $\boldsymbol{v}\in H^1_{loc}(\Omega\setminus\overline{D})$ *is given by (5.17).*

Proof. By virtue of the Betti's third formula (3.4c) and the Navier equation for the field $\overline{\boldsymbol{u}}$ in D, it can be shown that (5.20) admits the representation

$$\|\boldsymbol{u}\|^2_{H^1(D)}=\int_{\partial D}\left[\boldsymbol{v}(\boldsymbol{\xi})\cdot\boldsymbol{t}(\boldsymbol{\xi};\boldsymbol{u})-\boldsymbol{u}(\boldsymbol{\xi})\cdot\boldsymbol{t}_+(\boldsymbol{\xi};\boldsymbol{v})\right]dS_{\boldsymbol{\xi}},\quad \boldsymbol{u}\in\mathbb{H}(D). \tag{5.22}$$

The statement of the lemma readily follows from (5.22) and the denseness argument. □

THEOREM 5.5. *The space of single-layer potentials* $\{\boldsymbol{Sh},\ \boldsymbol{h}\in L_2(\Gamma_2)\}$ *given by (5.11) is dense in the space of classical solutions to the homogeneous Navier equation:* $\boldsymbol{Lu}+\rho\omega^2\boldsymbol{u}=\boldsymbol{0}$ *in* D *with respect to the* $H^1(D)$ *norm, i.e.* $\boldsymbol{S}\left(L_2(\Gamma_2)\right)$ *is dense with respect to the* $H^1(D)$ *norm in* $\overline{\mathbb{H}(D)}$.

Proof. Let $\boldsymbol{u}\in\overline{\mathbb{H}(D)}$ and assume that $(\boldsymbol{Sh},\boldsymbol{u})_{H^1(D)}=0$ for all $\boldsymbol{h}\in L_2(\Gamma_2)$. By Lemma 5.3, one can write $(\boldsymbol{h},\boldsymbol{S}^*\boldsymbol{u})_{L_2(\Gamma_2)}=0$ for all $\boldsymbol{h}\in L_2(\Gamma_2)$ and consequently $\boldsymbol{S}^*\boldsymbol{u}=\boldsymbol{0}$ on Γ_2, see (5.15). Now, by making use of the Holmgren's uniqueness theorem, one can conclude that $\boldsymbol{v}\equiv\boldsymbol{S}^*\boldsymbol{u}=\boldsymbol{0}$ in Ω^-. Finally it follows from Lemma 5.4 that $\|\boldsymbol{u}\|_{H^1(D)}=0$ and consequently $\boldsymbol{u}=\boldsymbol{0}$ in D. □

5.2. Existence and unboundedness of the solution. As examined earlier, the dual variant of the linear sampling method revolves around the equation of the first kind (4.1) (with $\boldsymbol{G}$ given by (4.5)) whose solution norm can be used as a characteristic function of the scatterer. The key hypotheses in this approach, however, are that (i) a unique solution to (4.1) exists for $\boldsymbol{z}\in\Omega_{\rm C}$ such that $\lim_{\boldsymbol{z}\to\boldsymbol{y}\in\Gamma}\|\boldsymbol{h}_{\boldsymbol{z},\boldsymbol{d}}\|_{L_2(\Gamma_2)}=\infty$, and (ii) there exists an approximate solution to (4.1) for $\boldsymbol{z}\in\Omega\setminus(\Omega_{\rm C}\cup\Gamma)$ such that $\lim_{\tau\to0}\|\boldsymbol{h}^{\tau}_{\boldsymbol{z},\boldsymbol{d}}\|_{L_2(\Gamma_2)}=\infty$ where τ is the approximation parameter. The validity of these assumptions is established next.

THEOREM 5.6. *Assume that (i)* $\boldsymbol{z}\in\Omega_{\rm C}$ *is fixed and* $\boldsymbol{d}\in\mathbb{R}^3$ *with* $\|\boldsymbol{d}\|=1$*; (ii)* Γ *is of class* $C^{1,\alpha}$*, and (iii)* $\rho\omega^2$ *is not a Neumann eigenvalue of* $-\boldsymbol{L}$ *in* $\Omega_{\rm C}$ *with eigenfunction* $\boldsymbol{Sh}$ *given by (5.11). Then* $\boldsymbol{G}$ *is one-to-one and for every* $\varepsilon>0$*, there exists* $\boldsymbol{h}(\cdot;\boldsymbol{z},\boldsymbol{d})\in L_2(\Gamma_2)$ *such that*

$$\left\|\boldsymbol{Gh}(\cdot;\boldsymbol{z},\boldsymbol{d})-\widehat{\boldsymbol{U}}(\cdot,\boldsymbol{z})\cdot\boldsymbol{d}\right\|_{L_2(\Gamma_1)}<\varepsilon, \tag{5.23}$$

where

$$\lim_{\boldsymbol{z}\to\boldsymbol{y}\in\Gamma}\|\boldsymbol{h}(\cdot;\boldsymbol{z},\boldsymbol{d})\|_{L_2(\Gamma_2)}=\infty. \tag{5.24}$$

Proof. To establish the injectivity of $\boldsymbol{G}$ assume the opposite, i.e. that $\boldsymbol{Gh}=\boldsymbol{0}$ has a non-trivial solution $\boldsymbol{h}$. By virtue of Theorem 5.1 and Theorem 5.5, it follows that there is a non-trivial solution $\boldsymbol{w}=\boldsymbol{Sh}$ to the homogeneous interior problem given by $\boldsymbol{Lw}+\rho\,\omega^2\boldsymbol{w}=\boldsymbol{0}$ in $\Omega_{\rm C}$ and $\boldsymbol{t}(\cdot;\boldsymbol{w})=\boldsymbol{0}$ on Γ, which violates hypothesis *(iii)* and thus establishes the first claim.

Next, consider the interior Neumann problem

$$\begin{aligned}&\boldsymbol{Lw}(\boldsymbol{x})+\rho\,\omega^2\boldsymbol{w}(\boldsymbol{x})=\boldsymbol{0},\quad \boldsymbol{x}\in\Omega_{\rm C},\\ &\boldsymbol{t}(\boldsymbol{x};\boldsymbol{w})+\widehat{\boldsymbol{T}}(\boldsymbol{x},\boldsymbol{z})\cdot\boldsymbol{d}=\boldsymbol{0},\quad \boldsymbol{x}\in\Gamma,\quad \boldsymbol{z}\in\Omega_{\rm C},\end{aligned} \tag{5.25}$$

in terms of $\boldsymbol{w}$. On the basis of the approximation property of elastic single-layer potentials $\boldsymbol{Sh}$ demonstrated in Theorem 5.5, it follows that $\boldsymbol{w}$ can be approximated arbitrarily close by a single-layer potential $\boldsymbol{Sh}$ with respect to the $H^1(\Omega_{\rm C})$ norm, i.e.

$$\|\boldsymbol{w}-\boldsymbol{Sh}(\cdot;\boldsymbol{z},\boldsymbol{d})\|_{H^1(\Omega_{\rm C})}<c_0\varepsilon,\quad \mathbb{R}\ni c_0>0. \tag{5.26}$$

Now, by virtue of the boundary condition (5.25b) and the trace theorem [26], one finds that

$$\|\widehat{\boldsymbol{T}}(\cdot,\boldsymbol{z})\cdot\boldsymbol{d}+\boldsymbol{t}(\cdot;\boldsymbol{Sh}(\cdot;\boldsymbol{z},\boldsymbol{d}))\|_{H^{-1/2}(\Gamma)}<c_1\varepsilon,\quad \mathbb{R}\ni c_1>0.$$

Claim (5.23) now directly follows from the above approximation properties and Theorem 5.1.

With the aid of the trace theorem and (5.26), there exists a positive constant $\mathbb{R}\ni c_2>0$ such that

$$\|\widehat{\boldsymbol{T}}(\cdot,\boldsymbol{z})\cdot\boldsymbol{d}\|_{H^{-1/2}(\Gamma)}\le c_2\,\|\boldsymbol{w}\|_{H^1(\Omega_{\rm C})}\le c_2\left(c_0\varepsilon+\|\boldsymbol{Sh}(\cdot;\boldsymbol{z},\boldsymbol{d})\|_{H^1(\Omega_{\rm C})}\right). \tag{5.27}$$

Since the single-layer integral operator $\boldsymbol{S}$ in (5.11) is bounded from $L_2(\Gamma_2)\to H^1(\Omega_{\rm C})$, there is a real constant $c_3>0$ such that

$$\|\boldsymbol{Sh}(\cdot;\boldsymbol{z},\boldsymbol{d})\|_{H^1(\Omega_{\rm C})}\le c_3\|\boldsymbol{h}(\cdot;\boldsymbol{z},\boldsymbol{d})\|_{L_2(\Gamma_2)}. \tag{5.28}$$

With (5.27), (5.28) and the limiting property of the elastodynamic (traction) half-space Green's functions [29]

$$\lim_{\boldsymbol{z}\to\boldsymbol{y}\in\Gamma}\|\widehat{\boldsymbol{T}}(\cdot,\boldsymbol{z})\cdot\boldsymbol{d}\|_{H^{-1/2}(\Gamma)}=\infty, \tag{5.29}$$

the second claim of the theorem, given by (5.24), immediately follows. □

To examine the case when $\boldsymbol{z}\in\Omega^-$, consider the perturbed scatterer domain $\widetilde{\Omega}_{{\rm C},\tau}=\Omega_{\rm C}\cup H_\tau\cup B^+_\tau(\boldsymbol{z})$ in Fig. 4.1b, where B^+_τ is a semi-ball of diameter $\tau>0$ centered at $\boldsymbol{z}$, and H_τ is a cylinder-like domain of diameter τ^2 smoothly connecting $\Omega_{\rm C}$ and $B^+_\tau(\boldsymbol{z})$. Next, let Γ and $\widetilde{\Gamma}_\tau$ signify the respective boundaries of $\Omega_{\rm C}$ and $\widetilde{\Omega}_{{\rm C},\tau}$, so that $\Gamma_\tau=\widetilde{\Gamma}_\tau\setminus(\Gamma\cap\widetilde{\Gamma}_\tau)$ is the external boundary of the appendage in Fig. 4.1b. With such premise, it is useful to consider the integral equation

$$\int_{\Gamma_2}\left[\widetilde{\boldsymbol{U}}(\boldsymbol{\xi},\boldsymbol{x})\;+\;\widetilde{\boldsymbol{V}}_\tau(\boldsymbol{\xi},\boldsymbol{x})\right]^{\rm T}\cdot\widetilde{\boldsymbol{h}}^\tau_{\boldsymbol{z},\boldsymbol{d}}(\boldsymbol{\xi})\,dS_{\boldsymbol{\xi}}\;=\;\widehat{\boldsymbol{U}}(\boldsymbol{x},\boldsymbol{z})\cdot\boldsymbol{d},\quad \boldsymbol{x}\in\Gamma_1,\quad \boldsymbol{z}\in\widetilde{\Omega}_{{\rm C},\tau}\subset\Omega,$$

introduced as a perturbation of (4.1) where $\widetilde{\boldsymbol{U}}$ is the "original" scattered tensor, induced by $\Omega_{\rm C}$, and $\widetilde{\boldsymbol{U}}+\widetilde{\boldsymbol{V}}_\tau$ is the perturbed scattered tensor induced by $\widetilde{\Omega}_{{\rm C},\tau}\subset\Omega$.

THEOREM 5.7. *Let $\boldsymbol{z}\in\Omega^-$ be fixed, and $\boldsymbol{d}\in\mathbb{R}^3$ with $\|\boldsymbol{d}\|=1$. Then, for every $\varepsilon>0$, there exists a perturbed density $\widetilde{\boldsymbol{h}}^\tau_{\boldsymbol{z},\boldsymbol{d}}\in L_2(\Gamma_2)$, $\tau>0$, such that*

$$\left\|\int_{\Gamma_2}\left[\widetilde{\boldsymbol{U}}(\boldsymbol{\xi},\cdot)\;+\;\widetilde{\boldsymbol{V}}_\tau(\boldsymbol{\xi},\cdot)\right]^{\rm T}\cdot\widetilde{\boldsymbol{h}}^\tau_{\boldsymbol{z},\boldsymbol{d}}(\boldsymbol{\xi})\,dS_{\boldsymbol{\xi}}-\widehat{\boldsymbol{U}}(\cdot,\boldsymbol{z})\cdot\boldsymbol{d}\right\|_{L_2(\Gamma_1)}<\varepsilon, \tag{5.30}$$

where

$$\lim_{\tau\to0}\|\widetilde{\boldsymbol{h}}^\tau_{\boldsymbol{z},\boldsymbol{d}}\|_{L_2(\Gamma_2)}=\infty\quad\textit{and}\quad\lim_{\tau\to0}\widetilde{\boldsymbol{V}}_\tau(\boldsymbol{\xi},\cdot)=\boldsymbol{0}. \tag{5.31}$$

Proof. With the assumption that $\boldsymbol{z} \in \widetilde{\Omega}_{\mathrm{C},\tau} \subset \Omega$ is fixed, it follows from Theorem 5.6 that there exists a solution $\widetilde{\boldsymbol{h}}^{\tau}_{\boldsymbol{z},\boldsymbol{d}} \in L_2(\Gamma_2)$ that satisfies the inequality (5.30). Next, on interchanging the limits $\boldsymbol{z} \to \boldsymbol{y} \in \widetilde{\Gamma}_\tau$ and $\tau \to 0$, one can conclude from (5.24) that $\lim\limits_{\tau \to 0} \|\widetilde{\boldsymbol{h}}^{\tau}_{\boldsymbol{z},\boldsymbol{d}}\|_{L_2(\Gamma_2)} = \infty$.

To demonstrate that $\lim_{\tau \to 0} \widetilde{\boldsymbol{V}}_\tau(\boldsymbol{\xi}, \cdot) = \boldsymbol{0}$, it is useful to employ an integral representation of the *perturbed* scattered field $\widetilde{\boldsymbol{U}}_\tau(\boldsymbol{\xi}, \boldsymbol{x}) \equiv \widetilde{\boldsymbol{U}}(\boldsymbol{\xi}, \boldsymbol{x}) + \widetilde{\boldsymbol{V}}_\tau(\boldsymbol{\xi}, \boldsymbol{x}),\ \boldsymbol{\xi} \in \Gamma_2,\ \boldsymbol{x} \in \Gamma_1$ over the perturbed boundary $\widetilde{\Gamma}_\tau$ and write an estimate of the perturbation $\widetilde{\boldsymbol{V}}_\tau(\boldsymbol{\xi}, \boldsymbol{x})$ in terms of τ. The complete proof is omitted here for brevity and can be found in [29]. ∎

6. Computational treatment and regularization. On the basis of the foregoing developments, elastic-wave reconstruction of impenetrable obstacles in a semi-infinite solid can be achieved by solving the integral equation (4.1) with the near-field operator $\boldsymbol{G}$ given by (4.5); a format that may be especially useful in situations involving a limited density of "illuminating" point sources acting over $\Gamma_1 \subset \Sigma$ (see Fig. 2.1). In the approach, the half-space is probed in a point-wise fashion by placing a fictitious point source (acting in direction $\boldsymbol{d}$) at *sampling* point $\boldsymbol{z} \in D \subset \Omega$, where D is the subsurface region of interest. On solving (4.1) over the pre-selected grid of sampling points, the spatial distribution of $1/\|\boldsymbol{h}(\cdot; \boldsymbol{z}, \boldsymbol{d})\|_{L_2(\Gamma_2)}$ can then be directly used to reconstruct the obstacle through regions where $1/\|\boldsymbol{h}\|_{L_2(\Gamma_2)}$ takes non-zero values.

In what follows, let the sampling point $\boldsymbol{z} \in D$ and the fictitious point-force direction $\boldsymbol{d}$ be fixed. With reference to (4.1), the unknown scatterer Ω_{C} can thus be reconstructed by solving the linear operator equation

$$\boldsymbol{G}\boldsymbol{h} = \boldsymbol{b}, \tag{6.1}$$

where $\boldsymbol{G}$ is given by (4.5), $\boldsymbol{h} = \boldsymbol{h}(\cdot; \boldsymbol{z}, \boldsymbol{d})$, and $\boldsymbol{b} = \widehat{\boldsymbol{U}}(\cdot, \boldsymbol{z}) \cdot \boldsymbol{d}$. As elucidated earlier, Fredholm integral equation of the first kind (6.1) constitutes an ill-posed mathematical problem in the sense of Hadamard [19, 21]. On citing the solvability of (6.1) as examined in Section 5, a careful numerical treatment must be adopted next to obtain a stable solution in terms of $\boldsymbol{h}$.

6.1. Discretization. In practice the input data, herein synthesized in the form of a scattered tensor field $\widetilde{\boldsymbol{U}}$, are monitored over a discrete set of control points located on the measurement surface Γ_2. Likewise, the seismic excitation used to illuminate the obstacle is provided by a finite number of "point" sources acting sequentially on the source surface Γ_1.

To consistently deal with such a discrete experimental input, let $\{E_k\}_{k=1}^K$ be a system of closed and non-overlapping subsets of the receiver surface Γ_2 such that $\Gamma_2 = \bigcup_{k=1}^K E_k$. On assuming that each subset E_k can be parametrized by a mapping $E \to E_k$ that introduces local coordinates, $\boldsymbol{\eta} = (\eta^1, \eta^2) \in E$, on $E_k \subset \Gamma_2$ where E is a polygonal domain in $\mathbb{R}^2$, the interpolation formula for a Q-noded approximation, E_k^a, of a generic surface element $E_k \subset \Gamma_2$ can be written as

$$\boldsymbol{\xi}(\boldsymbol{\eta}) \ = \ \sum_{q=1}^{Q} \psi_q(\boldsymbol{\eta})\, \boldsymbol{\xi}^q, \qquad \boldsymbol{\xi} \in E_k^a, \quad \boldsymbol{\xi}^q \in E_k, \quad \boldsymbol{\eta} \in E.$$

Here $\psi_q(\boldsymbol{\eta})$ are the Lagrange interpolation polynomials (shape functions) for the Q-noded element E_k^a with parent domain E, and $\boldsymbol{\xi}^q$ are the nodal points on E_k. Ac-

cordingly $\Gamma_2^a = \bigcup_{k=1}^K E_k^a$ is an approximation of Γ_2 so that the scattered tensor field $\widetilde{\boldsymbol{U}}$ and distribution $\boldsymbol{h}$ featured in (6.1) can be approximated over E_k^a as

$$\widetilde{\boldsymbol{U}}(\boldsymbol{\xi}(\boldsymbol{\eta}),\boldsymbol{x}) = \sum_{p=1}^{Q} \psi_p(\boldsymbol{\eta})\, \widetilde{\boldsymbol{U}}(\boldsymbol{\xi}^p,\boldsymbol{x}), \qquad \boldsymbol{h}_a(\boldsymbol{\xi}(\boldsymbol{\eta})) = \sum_{q=1}^{Q} \psi_q(\boldsymbol{\eta})\, \boldsymbol{h}^q, \qquad \boldsymbol{\xi}\in E_k^a,$$

where $\boldsymbol{h}^q = \boldsymbol{h}(\boldsymbol{\xi}^q)$ and $\boldsymbol{x}\in\Gamma_1$. In what follows, it is assumed that the values of the scattered tensor $\widetilde{\boldsymbol{U}}(\boldsymbol{\xi},\boldsymbol{x})$ are sampled over N_s source points $\{\boldsymbol{x}^j\}_1^{N_s}$ on Γ_1 and N_o observation points $\{\boldsymbol{\xi}^l\}_1^{N_o}$ on Γ_2. In this setting, an approximation of the near-field operator $\boldsymbol{G}$ over Γ_1 can be written as

$$(\boldsymbol{G}_a\boldsymbol{h}_a)(\boldsymbol{x}) = \sum_{k=1}^{K}\sum_{q=1}^{Q}\sum_{p=1}^{Q} \left[\widetilde{\boldsymbol{U}}(\boldsymbol{\xi}^{p_k},\boldsymbol{x})\right]^{\mathrm{T}} \cdot \boldsymbol{h}^{q_k} \int_{E_k^a} \psi_q(\boldsymbol{\eta})\,\psi_p(\boldsymbol{\eta})\, J d\eta^1 d\eta^2, \quad \boldsymbol{x}\in\Gamma_1, \tag{6.2}$$

where $J = J(\boldsymbol{\eta})$ is the Jacobian of transformation (6.2), while p_k and q_k are the respective global indices of the p-th and q-th element nodes on E_k^a. On the basis of (6.2) and a set of collocation points $\{\boldsymbol{x}^j\}_1^{N_s}\subset\Gamma_1$, a discretized form of the near-field integral equation (6.1) can be written as

$$\boldsymbol{G}_a\boldsymbol{h}_a = \boldsymbol{b}_a, \tag{6.3}$$

where $\boldsymbol{h}_a = (h_1^1, h_2^1, h_3^1, \ldots, h_1^{N_o}, h_2^{N_o}, h_3^{N_o})^{\mathrm{T}}$ is a vector containing the nodal values of $\boldsymbol{h}$ on Γ_2; $\boldsymbol{b}_a = (\widehat{\boldsymbol{U}}(\boldsymbol{x}^1,\boldsymbol{z})\cdot\boldsymbol{d}, \widehat{\boldsymbol{U}}(\boldsymbol{x}^2,\boldsymbol{z})\cdot\boldsymbol{d}, \ldots, \widehat{\boldsymbol{U}}(\boldsymbol{x}^{N_s},\boldsymbol{z})\cdot\boldsymbol{d})^{\mathrm{T}}$, and $\boldsymbol{G}_a\in\mathbb{C}^{3N_s\times 3N_o}$ is a finite-dimensional approximation of the near-field operator $\boldsymbol{G}$ following (6.2) wherein the surface integrals are approximated via a product Gauss-Legendre quadrature.

In view of the ill-posed nature of (6.1), a suitable regularization is necessary to obtain a stable approximate solution of (6.3). To this end, let ε be an a priori estimate of the measurement and numerical errors characterizing $\boldsymbol{G}_a$ so that

$$\|\boldsymbol{G}-\boldsymbol{G}_a\|_{L_2(\Gamma_1)} \le \varepsilon, \qquad \varepsilon = \gamma\|\boldsymbol{G}_a\|_{L_2(\Gamma_1)}, \qquad \gamma>0, \tag{6.4}$$

and let the right-hand side $\boldsymbol{b}$, polluted with numerical inaccuracies, be known up to an error δ whereby

$$\|\boldsymbol{b}-\boldsymbol{b}_a\|_{L_2(\Gamma_1)} \le \delta, \qquad \delta = \beta\|\boldsymbol{b}_a\|_{L_2(\Gamma_1)}, \qquad \beta>0. \tag{6.5}$$

In the ensuing (regularized) solution of the discrete system (6.3), Euclidean norm $\|\cdot\|$ in $\mathbb{C}^N$ induced by the inner product

$$(\boldsymbol{u},\boldsymbol{v}) = \sum_{i=1}^{N} \bar{u}_i v_i, \quad \boldsymbol{u},\boldsymbol{v}\in\mathbb{C}^N, \tag{6.6}$$

will be assumed where N is an appropriate dimension.

6.2. Tikhonov regularization. The Tikhonov regularization method [19, 36] replaces (6.3) with an equation of the second kind

$$\boldsymbol{G}_a^*\boldsymbol{G}_a\boldsymbol{h}_a^\alpha + \alpha\boldsymbol{h}_a^\alpha = \boldsymbol{G}_a^*\boldsymbol{b}_a, \qquad \boldsymbol{h}_a\in\mathbb{C}^{3N_o} \tag{6.7}$$

where $\boldsymbol{G}_a^*$ denotes the conjugate transpose of $\boldsymbol{G}_a$, $\alpha>0$ is the regularization parameter, and $\boldsymbol{h}_a^\alpha$ defacto minimizes the functional $J_\alpha(\boldsymbol{h}_a) = \|\boldsymbol{G}_a\boldsymbol{h}_a-\boldsymbol{b}_a\|^2 + \alpha\|\boldsymbol{h}_a\|^2$.

On employing the singular value decomposition of $\boldsymbol{G}_a$, it can be shown [11, 21] that the regularized solution $\boldsymbol{h}_a^\alpha$ of (6.7) and its squared norm admit the representation

$$\boldsymbol{h}_a^\alpha = \sum_{\nu_j>0} \frac{\nu_j}{\alpha+\nu_j^2}\,(\boldsymbol{u}_j,\boldsymbol{b}_a)\,\boldsymbol{v}_j, \qquad \|\boldsymbol{h}_a^\alpha\|^2 = \sum_{\nu_j>0} \frac{\nu_j^2}{\left(\alpha+\nu_j^2\right)^2}\,|(\boldsymbol{u}_j,\boldsymbol{b}_a)|^2\,. \tag{6.8}$$

Here $\boldsymbol{u}_i\in\mathbb{C}^{3N_s}$ $(i=1,2,\ldots 3N_s)$ and $\boldsymbol{v}_j\in\mathbb{C}^{3N_o}$ $(j=1,2,\ldots 3N_o)$ denote respectively the left and right singular vectors of $\boldsymbol{G}_a$, and $\nu_k\in\mathbb{R}$, $k=1,2,\ldots p=\min\{3N_s,3N_o\}$ are the singular values of $\boldsymbol{G}_a$ ordered so that $\nu_1\geq\nu_2\geq\cdots\geq\nu_p\geq 0$.

A method for choosing an optimal regularization parameter $\alpha=\alpha^*$, for which $\boldsymbol{h}_a^\alpha$ "closely" approximates the solution of (6.3), is given by the Morozov's discrepancy principle [19, 21, 25, 36]. In its most general form, the discrepancy principle due to Morozov states that the residual $\|\boldsymbol{G}_a\boldsymbol{h}_a^\alpha-\boldsymbol{b}_a\|$ should be commensurate to the errors characterizing the estimates of $\boldsymbol{G}$ and $\boldsymbol{b}$. With reference to (6.4)–(6.5), this implies

$$\|\boldsymbol{G}_a\boldsymbol{h}_a^\alpha-\boldsymbol{b}_a\| \;=\; \varepsilon\|\boldsymbol{h}_a^\alpha\|+\delta. \tag{6.9}$$

On assuming that $\delta\ll\varepsilon$ (the right-hand side, $\boldsymbol{b}=\widehat{\boldsymbol{U}}(\cdot,\boldsymbol{z})\cdot\boldsymbol{d}$, is a known analytic function of real variables), one can neglect numerical inaccuracies in the computation of the right-hand side $\boldsymbol{b}$ in (6.9) and define the discrepancy function as

$$\zeta(\alpha)=\|\boldsymbol{G}_a\boldsymbol{h}_a^\alpha-\boldsymbol{b}_a\|^2-\varepsilon^2\|\boldsymbol{h}_a^\alpha\|^2, \qquad \alpha>0. \tag{6.10}$$

On the basis of (6.8) and decomposition $\boldsymbol{b}_a=\sum\limits_{\nu_j>0}\boldsymbol{u}_j\,(\boldsymbol{u}_j,\boldsymbol{b}_a)$, the discrepancy function (6.10) and its derivative can be respectively rewritten as

$$\zeta(\alpha)=\sum_{\nu_j>0}\frac{\alpha^2-\varepsilon^2\nu_j^2}{\left(\alpha+\nu_j^2\right)^2}\,|(\boldsymbol{u}_j,\boldsymbol{b}_a)|^2\,, \qquad \zeta'(\alpha)=\sum_{\nu_j>0}\frac{2\nu_j^2(\alpha+\varepsilon^2)}{\left(\alpha+\nu_j^2\right)^3}\,|(\boldsymbol{u}_j,\boldsymbol{b}_a)|^2\,.$$

It is readily seen that $\zeta'(\alpha)>0,$ forl $\alpha\in(0,\infty)$, and hence the discrepancy function $\zeta(\alpha)$ is a monotonically increasing function. By virtue of the limit from above, asymptotic behavior $\lim_{\alpha\downarrow 0}\zeta(\alpha)<0$, and the monotonicity of ζ, it follows that $\zeta(\alpha)$ has a unique root, $\alpha^\star$, satisfying $\zeta(\alpha^\star)=0$ that can be computed using e.g. root-finding Newton's method.

6.3. Preconditioned conjugate gradient method. In situations where the singular value decomposition of $\boldsymbol{G}_a$ is not feasible, e.g. for "large" systems, the conjugate gradient (CG) method [18, 21] can be alternatively employed to solve (6.3) wherein the regularized iterative solution $\boldsymbol{h}_a^\kappa$ is found by minimizing the functional $J(\boldsymbol{h}_a)=\|\boldsymbol{G}_a\boldsymbol{h}_a-\boldsymbol{b}_a\|^2$. In the iteration procedure of the CG method, iteration number κ plays the role of the regularization parameter; accordingly, its optimal value, $\kappa=\kappa^\star$, is to be chosen by a suitable stopping rule. In this investigation, a preconditioned conjugate gradient method proposed by Santos [34] will be used. Rooted in [4], this technique can be briefly described using the decomposition $\boldsymbol{G}_a\boldsymbol{G}_a^*=\boldsymbol{T}+\boldsymbol{D}+\boldsymbol{T}^*$, where $\boldsymbol{T}$ is strictly lower triangular, $\boldsymbol{D}=\mathrm{diag}(d_1,d_2,\ldots,d_{3N_s})$, and $d_i\in\mathbb{R}$ is the diagonal element of $\boldsymbol{G}_a\boldsymbol{G}_a^*\in\mathbb{C}^{3N_s\times 3N_s}$. With such definitions, let

$$\boldsymbol{C}_\tau=(\boldsymbol{D}+\tau\,\boldsymbol{T})\boldsymbol{D}^{-1/2}, \tag{6.11}$$

form a basis for the preconditioner where $\tau\in[0,2]$ is a relaxation parameter. In this setting, the regularized solution $\boldsymbol{h}_a^\kappa$ of (6.3) can be found by minimizing the functional

$$J_C(\boldsymbol{h}_a)=\|\boldsymbol{C}_\tau^{-1}(\boldsymbol{G}_a\boldsymbol{h}_a-\boldsymbol{b}_a)\|^2, \quad \boldsymbol{h}_a\in\mathbb{C}^{3N_o},$$

i.e. by solving the the normal equation

$$\boldsymbol{G}_a^* \boldsymbol{C}_\tau^{-*} \boldsymbol{C}_\tau^{-1} \boldsymbol{G}_a \boldsymbol{h}_a \;=\; \boldsymbol{G}_a^* \boldsymbol{C}_\tau^{-*} \boldsymbol{C}_\tau^{-1} \boldsymbol{b}_a \tag{6.12}$$

where $\boldsymbol{C}_\tau^{-*} = (\boldsymbol{C}_\tau^{-1})^*$. A modification of the CG algorithm (PCCGNR) [34] for solving (6.12), wherein the "net" residual $\boldsymbol{z}^\kappa = \boldsymbol{b}_a - \boldsymbol{G}_a \boldsymbol{h}_a^\kappa$ is computed at every iterate κ, can be written as

Algorithm 6.1.

Given $\boldsymbol{h}_a^0$:

Set $\boldsymbol{z}^0 = \boldsymbol{b}_a - \boldsymbol{G}_a \boldsymbol{h}_a^0, \quad \boldsymbol{r}_0 = \boldsymbol{G}_a^* \boldsymbol{C}_\tau^{-*} \boldsymbol{C}_\tau^{-1} \boldsymbol{z}^0, \quad \boldsymbol{p}^0 = \boldsymbol{r}^0.$

For $\kappa = 0, 1, \ldots$

$$\boldsymbol{g}^\kappa = \boldsymbol{G}_a \, \boldsymbol{p}^\kappa, \quad \boldsymbol{q}^\kappa = \boldsymbol{C}_\tau^{-1} \boldsymbol{g}^\kappa$$

$$\alpha_\kappa = \frac{\|\boldsymbol{r}^\kappa\|^2}{\|\boldsymbol{q}^\kappa\|^2}$$

$$\boldsymbol{h}_a^{\kappa+1} = \boldsymbol{h}_a^\kappa + \alpha_\kappa \, \boldsymbol{p}^\kappa$$

$$\boldsymbol{z}^{\kappa+1} = \boldsymbol{z}^\kappa - \alpha_\kappa \, \boldsymbol{g}^\kappa, \quad \boldsymbol{r}^{\kappa+1} = \boldsymbol{G}_a^* \boldsymbol{C}_\tau^{-*} \boldsymbol{C}_\tau^{-1} \boldsymbol{z}^{\kappa+1}$$

$$\beta_\kappa = \frac{\|\boldsymbol{r}^{\kappa+1}\|^2}{\|\boldsymbol{r}^\kappa\|^2}$$

$$\boldsymbol{p}^{\kappa+1} = \boldsymbol{r}^{\kappa+1} + \beta_\kappa \, \boldsymbol{p}^\kappa$$

For an efficient implementation of Algorithm 6.1, it is desirable to compute the products $\boldsymbol{C}_\tau^{-1} \boldsymbol{g}$ and $\boldsymbol{C}_\tau^{-*} \boldsymbol{w}$ without calculating the inverse of (6.11) explicitly. To this end, let $\boldsymbol{f}_i \in \mathbb{C}^{3N_o}$ denote the ith row of $\boldsymbol{G}_a$, and let $d_i = (\boldsymbol{f}_i, \boldsymbol{f}_i)$ be the ith diagonal entry of $\boldsymbol{D} = \mathrm{diag}(d_1, d_2, \ldots, d_{3N_s})$, where the inner product $(\cdot, \cdot)$ is given by (6.6). With such definitions, the components of $\boldsymbol{q} = \boldsymbol{C}_\tau^{-1} \boldsymbol{g}$ can be computed in a recursive fashion [4, 34] as

$$q_i = d_i^{-1/2} (g_i - \tau \, (\boldsymbol{a}_i, \boldsymbol{f}_i)) \,, \qquad \boldsymbol{a}_{i+1} = \boldsymbol{a}_i + d_i^{-1/2} \, \overline{q}_i \, \boldsymbol{f}_i. \qquad i = 1, 2, \ldots, 3N_s.$$

where $\mathbb{C}^{3N_o} \ni \boldsymbol{a}_1 = \boldsymbol{0}$ initializes the procedure. Similarly by letting $\mathbb{C}^{3N_o} \ni \boldsymbol{a}_{3N_s} = \boldsymbol{0}$, the components of $\boldsymbol{s} = \boldsymbol{C}_\tau^{-*} \boldsymbol{w}$ can be computed as

$$s_i = d_i^{-1/2} w_i - \tau \, d_i^{-1} (\boldsymbol{a}_i, \boldsymbol{f}_i), \qquad \boldsymbol{a}_{i-1} = \boldsymbol{a}_i + \overline{s}_i \, \boldsymbol{f}_i, \qquad i = 3N_s, 3N_s - 1, \ldots, 1.$$

The selection of an optimal iteration number (regularization parameter) $\kappa = \kappa^\star$ in Algorithm 6.1 is rather heuristic. As mentioned in [35], generalization of the discrepancy principle manifest in (6.10) to CG-type methods is still an open question. Nevertheless, one may by analogy to (6.10) introduce the discrepancy function as

$$\zeta(\kappa) = \|\boldsymbol{G}_a \, \boldsymbol{h}_a^\kappa - \boldsymbol{b}_a\|^2 - \varepsilon^2 \|\boldsymbol{h}_a^\kappa\|^2, \quad \kappa \in \mathbb{N} \cup \{0\}. \tag{6.13}$$

By virtue of (6.13), one can select the optimal iteration number $\kappa^\star$ as the number κ that corresponds to the minimum of $|\zeta(\kappa)|$; a quantity whose computation at every iterate is facilitated by the computation of the "net" residual $\boldsymbol{z}^\kappa$ in Algorithm 6.1.

7. Results. On the basis of the foregoing developments, the task of reconstructing an obstacle $\Omega_{\rm C}$ in a semi-infinite solid Ω from near-field elastic waveforms (Fig. 2.1) can be achieved by solving the integral equation (4.1) over a reference sampling region $D \supset \Omega_{\rm C}$ by means of the featured regularization methods. By introducing the grid of sampling points $\boldsymbol{z}^m \in D \subset \Omega$ $(m=1,2,\dots M)$ spanning the region of interest, the half-space is sequentially excited by the virtual point sources acting at $\boldsymbol{z}^m$ in direction $\boldsymbol{d}$, and $1/\|\boldsymbol{h}(\cdot;\boldsymbol{z}^m,\boldsymbol{d})\|_{L_2(\Gamma_2)}$ is plotted over the selected raster. As indicated in [11, 35] for acoustic problems, spatial distribution of the optimal regularization parameter α^* provided by Tikhonov regularization can be used as an alternative reconstruction tool. In what follows, plots of $\alpha^*(\boldsymbol{z}^m,\boldsymbol{d})$ will also be provided to investigate the latter possibility.

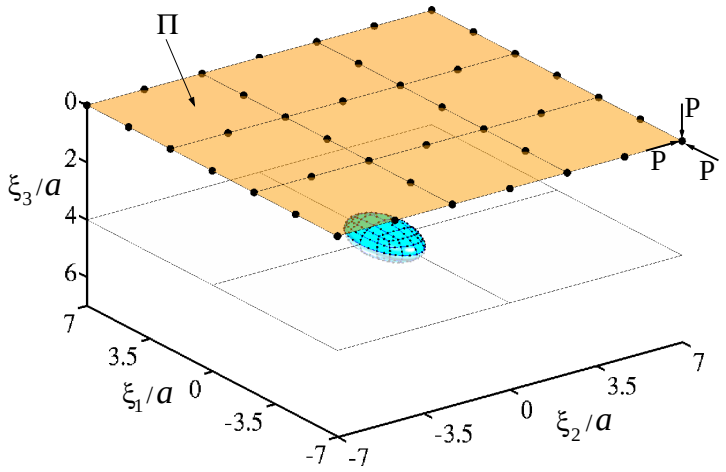

FIG. 7.1. *Ellipsoidal cavity and observation grid in the half-space* $\xi_3 > 0$.

7.1. Void imaging using triaxial seismic excitation. With reference to the Cartesian frame $\{O;\xi_1,\xi_2,\xi_3\}$ featured in Fig. 7.1, consider the problem of reconstructing an ellipsoidal cavity centered at $(0,0,4a)^{\rm T}$ whose semi-axes, of lengths $(1.8a,a,0.6a)^{\rm T}$, are aligned with the global coordinate system. Elastic properties of the half-space and the frequency of excitation are taken as

$$\mathbf{C} = \frac{3}{2}\mu\,\mathbf{I}_2 \otimes \mathbf{I}_2 \,+\, 2\,\mu\,\mathbf{I}_4, \quad \bar{\omega} = \frac{\omega\, a}{\sqrt{\mu/\rho}} = 1.8, \quad \mu > 0. \tag{7.1}$$

On assuming that the source surface Γ_1 and the observation surface Γ_2 coincide, i.e. $\Gamma_1 = \Gamma_2 = \Pi$, synthetic observations of the scattered tensor $\widetilde{\boldsymbol{U}}$ are generated via the elastodynamic boundary element method [30] by assuming $N_s = 25$ source points uniformly distributed over the test area $(14a \times 14a)$ as shown in Fig. 7.2. From every source point $\boldsymbol{x}^k$ on the grid $(k=1,2,\dots N_s)$, the half-space is illuminated using time-harmonic excitation of magnitude $P = 0.2\mu a^2$ in three perpendicular directions (ξ_1, ξ_2 and ξ_3) as illustrated in Fig. 7.1. For each $\boldsymbol{x}^k$, synthetic data $\widetilde{\boldsymbol{U}}(\boldsymbol{\xi}^j,\boldsymbol{x}^k)$, are computed over $N_o = 40$ receiver points $\boldsymbol{\xi}^j$ covering the same test area (see Fig. 7.2). To mimic the effect of measurement uncertainties, synthetic observations $\widetilde{\boldsymbol{U}}$ are corrupted as

$$\widetilde{\boldsymbol{U}}(\boldsymbol{\xi}^j,\boldsymbol{x}^k) \;:=\; (1+\varrho\chi)\,\widetilde{\boldsymbol{U}}(\boldsymbol{\xi}^j,\boldsymbol{x}^k), \qquad \begin{matrix} j=1,2,\dots N_o \\ k=1,2,\dots N_s \end{matrix} \tag{7.2}$$

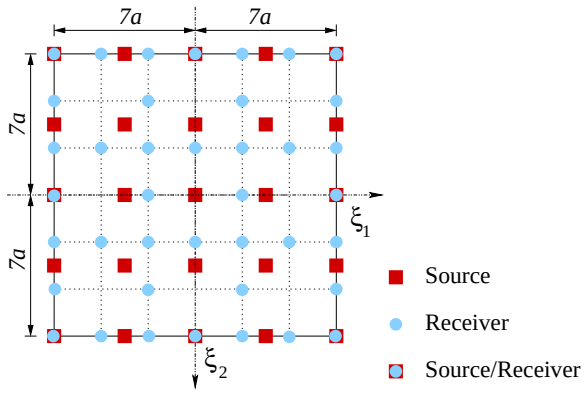

FIG. 7.2. *Testing surface* Π *with 25 sources and 40 receivers.*

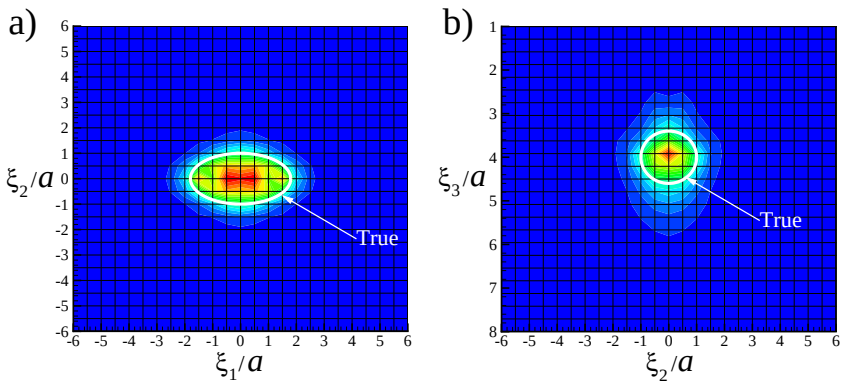

FIG. 7.3. *Distribution of* $1/\|\boldsymbol{h}_{\boldsymbol{z},\boldsymbol{d}}\|_{L_2(\Pi)}$ *across a) horizontal plane* $\xi_3 = 4a$*, and b) vertical plane* $\xi_1 = 0$*. TR method:* $\bar{\omega} = 1.8$*,* $\boldsymbol{d} = (1,0,0)^{\mathrm{T}}$*,* $\gamma = 10^{-7}$*,* $\varrho = 0$*.*

where ϱ is the noise amplitude, and χ is a random variable uniformly distributed over the interval $[-1,1]$. It is also important to point out that the testing rectangular surface area Π subtends a solid angle of only 3.42 sr at the center of the ellipsoidal void. This limited angle of view can make the reconstruction task difficult.

With the above problem parameters, the near-field equation (4.1) is discretized as examined in Section 6 and solved assuming $\boldsymbol{d} = (1,0,0)^{\mathrm{T}}$ for the density $\boldsymbol{h}_{\boldsymbol{z},\boldsymbol{d}}$ over a 25×25 grid of uniformly spaced sampling points in the horizontal plane $\xi_3 = 4a$ and vertical plane $\xi_1 = 0$. For completeness, the results are generated on the basis of both i) Tikhonov regularization (TR) method, and ii) preconditioned conjugate gradient (PCG) method. With reference to the discrepancy functions (6.10) and (6.13), an estimate ε of the "measurement" and numerical errors characterizing the near-field operator is computed as $\varepsilon = \gamma \|\boldsymbol{G}_a\|$, where $\|\boldsymbol{G}_a\|$ is given by the maximum singular value of $\boldsymbol{G}_a$ for the TR method and by the Frobenius norm [2] of $\boldsymbol{G}_a$ for the PCG method.

By setting $\gamma = 10^{-7}$ and assuming no noise on the measurements $\widetilde{\boldsymbol{U}}$ (i.e. $\varrho = 0$), Figs. 7.3 and 7.4 depict respectively the contour plots of $1/\|\boldsymbol{h}(\cdot;\boldsymbol{z},\boldsymbol{d})\|_{L_2(\Pi)}$ computed using the TR method and the PCG approach. While the respective graphs in the two figures are similar, it should be noted that the $\|\boldsymbol{h}\|$ data in Fig. 7.3 were computed in

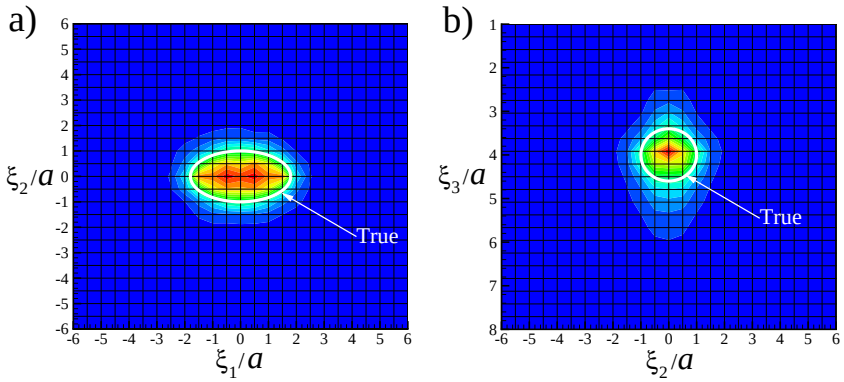

FIG. 7.4. *Distribution of* $1/\|\boldsymbol{h}_{\boldsymbol{z},\boldsymbol{d}}\|_{L_2(\Pi)}$ *across a) horizontal plane* $\xi_3 = 4a$*, and b) vertical plane* $\xi_1 = 0$*. PCG method:* $\bar{\omega} = 1.8$*,* $\boldsymbol{d} = (1,0,0)^{\mathrm{T}}$*,* $\tau = 0.5$*,* $\gamma = 10^{-7}$*,* $\varrho = 0$*.*

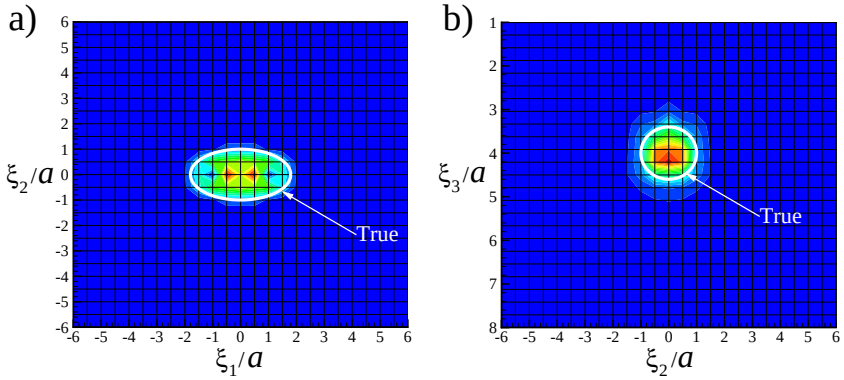

FIG. 7.5. *Distribution of* $1/\|\boldsymbol{h}_{\boldsymbol{z},\boldsymbol{d}}\|_{L_2(\Pi)}$ *across a) horizontal plane* $\xi_3 = 4a$*, and b) vertical plane* $\xi_1 = 0$*. TR method:* $\bar{\omega} = 1.8$*,* $\boldsymbol{d} = (1,0,0)^{\mathrm{T}}$*,* $\gamma = 10^{-12}$*,* $\varrho = 0$*.*

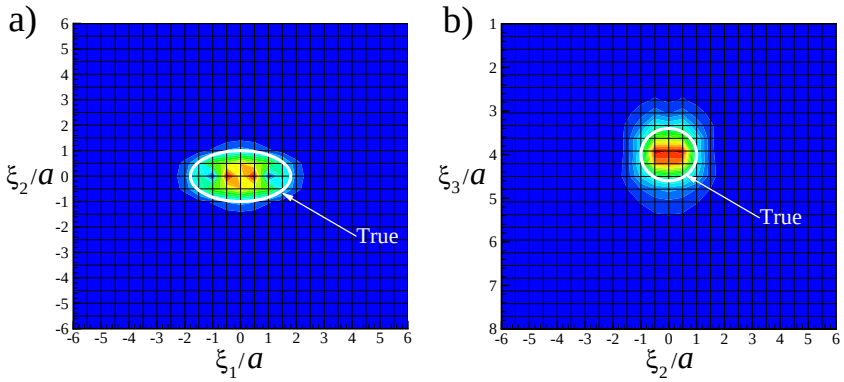

FIG. 7.6. *Distribution of* $1/\|\boldsymbol{h}_{\boldsymbol{z},\boldsymbol{d}}\|_{L_2(\Pi)}$ *across a) horizontal plane* $\xi_3 = 4a$*, and b) vertical plane* $\xi_1 = 0$*. PCG method:* $\bar{\omega} = 1.8$*,* $\boldsymbol{d} = (1,0,0)^{\mathrm{T}}$*,* $\tau = 0.5$*,* $\gamma = 10^{-12}$*,* $\varrho = 0$*.*

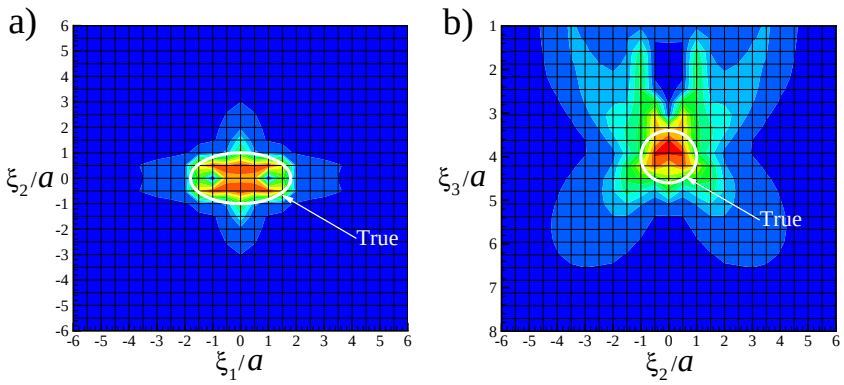

FIG. 7.7. *Distribution of* $\alpha^*(\boldsymbol{z},\boldsymbol{d})$ *stemming from the TR method across a) horizontal plane* $\xi_3=4a$*, and b) vertical plane* $\xi_1=0$*.* $\bar{\omega}=1.8$*,* $\boldsymbol{d}=(1,0,0)^{\mathrm{T}}$*,* $\gamma=10^{-7}$*,* $\varrho=0$*.*

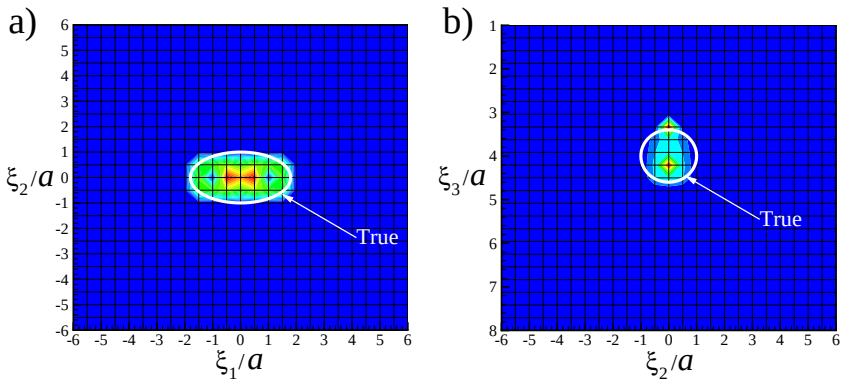

FIG. 7.8. *Distribution of* $\alpha^*(\boldsymbol{z},\boldsymbol{d})$ *stemming from the TR method across a) horizontal plane* $\xi_3=4a$*, and b) vertical plane* $\xi_1=0$*.* $\bar{\omega}=1.8$*,* $\boldsymbol{d}=(1,0,0)^{\mathrm{T}}$*,* $\gamma=10^{-12}$*,* $\varrho=0$*.*

approximately 4 minutes as compared to 34 minutes needed for Fig. 7.4 (both computations were performed on a Linux system with 2 Intel Xeon processors running at 2GHz). Such "discrepancy" stems from the fact that the singular value decomposition underlying TR is performed only *once* per graph whereas Algorithm 6.1 is required at *every* sampling point. For elastic-wave imaging applications involving large amounts of observations (e.g. volumetric motion data obtained via magnetic resonance methods [20, 13]), however, the PCG method is expected to be far more competitive from the computational point of view.

Regarding the fidelity of elastic-wave reconstruction, numerical experiments have further shown that the results presented in Figs. 7.3 and 7.4 can be improved if the modeling error estimate, $\varepsilon=\gamma\|\boldsymbol{G}_a\|$, is selected more appropriately. To illustrate this observation, Figs. 7.5 and 7.6 illustrate the respective distributions of $1/\|\boldsymbol{h}(\cdot;\boldsymbol{z},\boldsymbol{d})\|_{L_2(\Pi)}$ assuming $\gamma=3\times10^{-12}$. Although again similar, the reconstruction by the PCG method in Fig. 7.6 apparently has more artifacts than its TR counterpart shown in Fig. 7.5.

Following the earlier discussion, performance of the optimal regularization param-

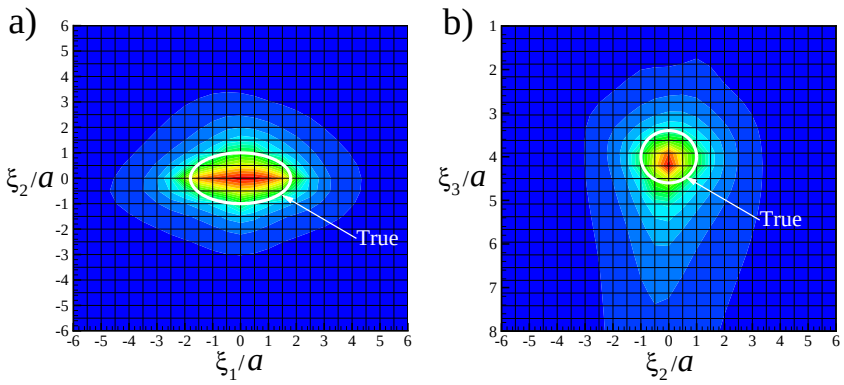

FIG. 7.9. *Distribution of* $1/\|\boldsymbol{h}_{\boldsymbol{z},\boldsymbol{d}}\|_{L_2(\Pi)}$ *across a) horizontal plane* $\xi_3 = 4a$*, and b) vertical plane* $\xi_1 = 0$*. TR method:* $\bar{\omega} = 1.8$*,* $\boldsymbol{d} = (1,0,0)^{\mathrm{T}}$*,* $\gamma = 3\times10^{-9}$*,* $\varrho = 0.01$*.*

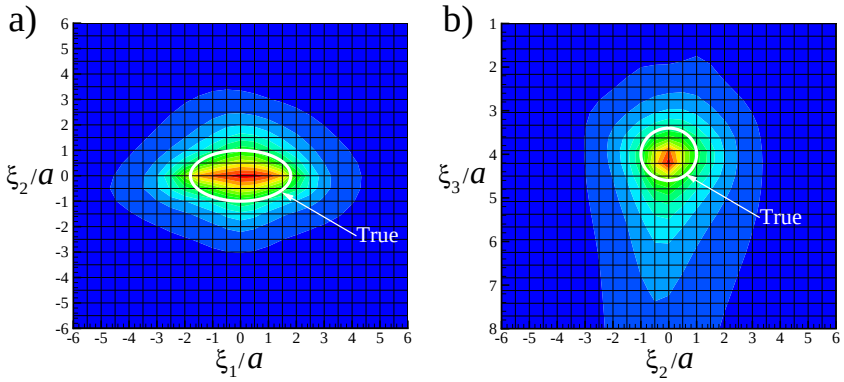

FIG. 7.10. *Distribution of* $1/|\boldsymbol{h}_{\boldsymbol{z},\boldsymbol{d}}\|_{L_2(\Pi)}$ *across a) horizontal plane* $\xi_3 = 4a$*, and b) vertical plane* $\xi_1 = 0$*. PCG method:* $\bar{\omega} = 1.8$*,* $\boldsymbol{d} = (1,0,0)^{\mathrm{T}}$*,* $\tau = 0.5$*,* $\gamma = 3\times10^{-9}$*,* $\varrho = 0.01$*.*

eter $\alpha^* = \alpha^*(\boldsymbol{z},\boldsymbol{d})$ stemming from TR is examined next. Its utility as an alternative reconstruction tool can be seen from Figs. 7.7 and 7.8 where the contour plots of $\alpha^*(\boldsymbol{z},\boldsymbol{d})$ are plotted respectively for $\gamma = 10^{-7}$ and $\gamma = 3\times10^{-12}$ over the featured sampling grid. As can be seen from Fig. 7.7, the reconstruction suffers from significant artifacts when the error estimate γ is not properly chosen.

To provide further insight into the performance of the linear sampling method, imaging problem in Fig. 7.1 is re-examined in the context of noise-polluted measurements $\boldsymbol{U}$ assuming $\varrho = 0.01$ in (7.2). The results of the TR method and the PCG method are shown respectively in Figs. 7.9 and 7.10, assuming $\gamma = 3\times10^{-9}$. As can be seen from the "smearing" of reconstructed images, both techniques are relatively sensitive to the input noise. For completeness, Fig. 7.11 plots the distribution of the optimal regularization parameter $\alpha^* = \alpha^*(\boldsymbol{z},\boldsymbol{d})$ over the search grid for $\gamma = 3\times10^{-9}$ and $\varrho = 0.01$. It is apparent from the plot that the region containing the scatterer is predicted well relative to its solution-norm counterparts in Figs. 7.9 and 7.10, thus highlighting the potential of the α-distribution as a reconstruction tool in physical situations involving inevitable measurement noise.

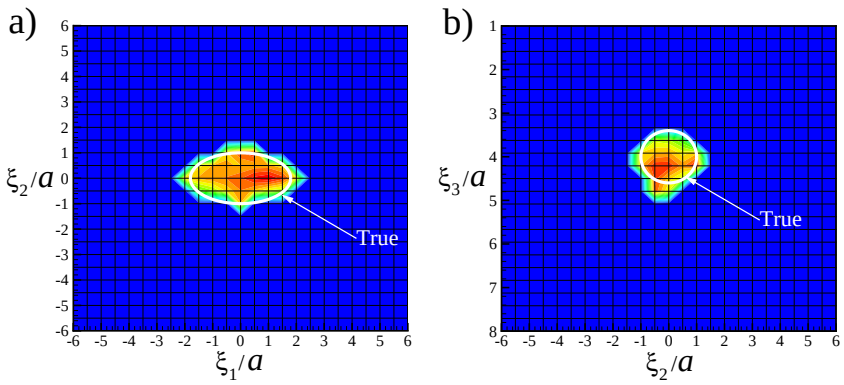

FIG. 7.11. *Distribution of* $\alpha^*(\boldsymbol{z},\boldsymbol{d})$ *stemming from the TR method across a) horizontal plane* $\xi_3=4a$*, and b) vertical plane* $\xi_1=0$*.* $\bar{\omega}=1.8$*,* $\boldsymbol{d}=(1,0,0)^{\mathrm{T}}$*,* $\gamma=10^{-9}$*,* $\varrho=0.01$*.*

8. Summary. In this study, a three-dimensional inverse problem involving near-field elastic-wave reconstruction of impenetrable obstacles in a semi-infinite solid is examined in the context of a regularized sampling method. To cater for active imaging configurations characterized a limited density of excitation sources, an adjoint formulation of the near-field LSM is established that features a linear integral equation of the first kind involving integration over the *measurement* (as opposed to the source) surface. To deal with its ill-posed nature, the equation is solved by alternative means of Tikhonov regularization and a preconditioned conjugate gradient method. Computational details of the imaging technique, including evaluation of the featured integrals as well as the implementation of regularization strategies, are highlighted. An example dealing with the reconstruction of an ellipsoidal void from noise-polluted synthetic measurements is included to illustrate the effectiveness of proposed developments. Numerical results indicate a similar performance of both regularization methods, characterized by i) a potential for three-dimensional obstacle reconstruction from limited-aperture measurements, and ii) notable sensitivity to measurement noise.

Acknowledgments. The support provided by the National Science Foundation grant CMS-324348 to B. Guzina and the University of Minnesota Supercomputing Institute during the course of this investigation is gratefully acknowledged.

REFERENCES

[1] T. Arens, Linear sampling methods for 2D inverse elastic wave scattering, *Inverse Problems* **17** (2001) 1445–1464.
[2] O. Axelsson, *Iterative Solution Methods* (Cambridge University Press, Cambridge, 1994).
[3] M. Bonnet, BIE and material differentiation applied to the formulation of obstacle inverse problems, *Eng. Anal. with Bound. Elem.* **15** (1995) 121–136.
[4] A. Björck and T. Elfving, Accelerated projection methods for computing pseudoinverse solutions of systems of linear equations, *BIT* **19** (1979) 145–163.
[5] C. Bunks, F. M. Saleck, S. Zaleski, and G. Chavent, Multiscale seismic waveform inversion, *Geophysics*, **60** (1995) 1457–1473.
[6] A. Charalambopoulos, D. Gintides and K. Kiriaki K, The linear sampling method for the transmission problem in three-dimensional linear elasticity, *Inverse Problems* **18** (2002) 547–558.

[7] D. Colton and R. Kress, *Integral Equation Method in Scattering Theory* (Wiley, New York, 1983).
[8] D. Colton and A. Kirsch, A simple method for solving inverse scattering problems in the resonance region, *Inverse Problems* **12** (1996) 383–393.
[9] D. Colton and R. Kress, *Inverse Acoustic and Electromagnetic Scattering Theory* (Springer, Berlin, 1998).
[10] D. Colton and P. Monk, Linear sampling method for the detection of leukemia using microwaves, *SIAM J. Appl. Math.* **58** (1998) 926–941.
[11] D. Colton, K. Giebermann and P. Monk, Regularized sampling method for solving three-dimensional inverse scattering problems, *SIAM J. Sci. Comput.* **21** (2000) 2316–2330.
[12] D. Colton, J. Coyle and P. Monk, Recent developments in inverse acoustic scattering theory, *SIAM Review* **42** (2000) 369–414.
[13] M.M. Doyley, S. Srinivasan, E. Dimidenko, N. Soni and J. Ophir, Enhancing the performance of model-based elastography by incorporating additional a priori information in the modulus image reconstruction process, *Phys. Med. Biol.*, **51** (2006) 95–112.
[14] Garabedian P R *Partial Differential Equations* (AMS Chelsea, Rhode Island, 1998)
[15] B. B. Guzina and R. Y. S. Pak, On the analysis of wave motions in a multi-layered solid, *Quart. J. Mech. Appl. Math.* **54** (2001) 13–37.
[16] B. B. Guzina, S. Nintcheu Fata and M. Bonnet, On the stress-wave imaging of cavities in a semi-infinite solid, *Int. J. Solids Struct.* **40** (2003) 1505–1523.
[17] B. B. Guzina and M. Bonnet, Topological derivative for the inverse scattering of elastic waves, *Quart. J. Mech. Appl. Math.* **57** (2004) 161–179.
[18] M. Hanke, *Conjugate Gradient type Methods for Ill-posed Problems*, Pitman Research Notes in Mathematics Series (Longman Scientific & Technical, Harlow, 1995).
[19] W. E. Heinz, M. Hanke and A. Neubauer, *Regularization of Inverse Problems* (Kluwer, Dordrecht, 1996).
[20] F.E. Kennedy, M.M. Doyley, E.E Van Houten, J.B. Weaver and K.D. Paulsen, Determination of in-vivo elastic properties of soft tissue using magnetic resonance elastography, *Advances in Bioengineering, ASME* **55** (2003) 327–328.
[21] A. Kirsch, *An Introduction to the Mathematical Theory of Inverse Problems* (Springer, Berlin, 1996).
[22] R. Kress, *Linear Integral Equation* (Springer, Berlin, 1999).
[23] V. D. Kupradze, *Three Dimensional Problems of the Mathematical Theory of Elasticity and Thermoelasticity* (North Holland, Amsterdam, 1979).
[24] W. McLean *Strongly Elliptic Systems and Boundary Integral Equations* (Cambridge: Cambridge University Press, 2000)
[25] V. A. Morozov, *Methods for Solving Incorrectly Posed Problems* (Springer, Berlin, 1984).
[26] J. C. Nédélec *Acoustic and Electromagnetic Equations* (Springer, Berlin, 2001)
[27] S. Nintcheu Fata, *3D Subterranean Imaging via Elastic waves* (PhD Thesis, University of Minnesota, 2003).
[28] S. Nintcheu Fata, B. B. Guzina and M. Bonnet, Computational framework for the BIE solution to inverse scattering problems in elastodynamics, *Comp. Mech.* **32** (2003) 370–80.
[29] S. Nintcheu Fata and B. B. Guzina, A linear sampling method for near-field inverse problems in elastodynamics, *Inverse Problems* **20** (2004) 713–736.
[30] R. Y. S. Pak and B. B. Guzina, Seismic soil-structure interaction analysis by direct boundary element methods, *Int. J. Solids Struct.* **36** (1999) 4743–4766.
[31] G. Pelekanos and V. Sevroglou, Inverse scattering by penetrable objects in two-dimensional elastodynamics *J. Comp. Appl. Math.* **151** (2003) 129–140.
[32] R. E. Plessix, Y. H. De Roeck, and G. Chavent, Waveform inversion of reflection seismic data for kinematic parameters by local optimization. *SIAM J. Sci. Comput.*, **20** (1998) 1033–1052.
[33] R. G. Pratt, F. C. Gao, C. Zelt and A. Levander, The limits and complementary nature of traveltime and waveform tomography *Proc. Int. Conf. on Sub-basalt Imaging*, Cambridge, England, 2002.
[34] R. J. Santos, Preconditioning conjugate gradient with symmetric algebraic reconstruction technique (ART) in computerized tomography, *Appl. Num. Math.* **47** (2003) 255–263.
[35] A. Tacchino, J. Coyle and M. Piana, Numerical validation of the linear sampling method, *Inverse Problems* **18** (2002) 511–527.
[36] A. N. Tikhonov, A. V. Goncharsky, V. V. Stepanov and A. G. Yagola, *Numerical Methods for the Solution of Ill-Posed Problems* (Kluwer, Dordrecht, 1995).